Journal of Petroleum Science and Engineering 220 (2023) 111178

Contents lists available at ScienceDirect

Journal of Petroleum Science and Engineering

journal homepage: www.elsevier.com/locate/petrol

Paleoenvironment-driven organic matter accumulation in lacustrine shale mixed with shell bioclasts: A case study from the Jurassic Da'anzhai member, Sichuan Basin (China)

Wenzhi Lei [a,b], Dongxia Chen [a,b,*], Ziyi Liu [a,b], Ming Cheng [a,b]

[a] State Key Laboratory of Petroleum Resources and Prospecting, China University of Petroleum, Beijing, 102200, China
[b] College of Geosciences, China University of Petroleum, Beijing, 102200, China

ARTICLE INFO

Keywords:
Lacustrine calcareous shale
Paleoenvironment
Geochemistry
Shell bioclasts
Da'anzhai member
Sichuan basin

ABSTRACT

The sedimentary environment governs the depositional processes, ecological environments, and hydrodynamics, which affect the accumulation of organic-rich sediments. Some particular issues are unsolved about the organic matter accumulations of lacustrine shale mixed with shell bioclasts due to their alternating deposition. Freshwater bivalve remains are a familiar constituent of the Da'anzhai lacustrine calcareous shale, which indicates enhanced activities of benthic organisms. Under this background, favorable environmental conditions for the deposition and preservation of abundant organic matter may be different from classical models. Total organic carbon and elemental concentration analyses of lacustrine calcareous shale samples from the Jurassic Da'anzhai Member in the Sichuan Basin were carried out to reconstruct the paleoenvironment and reveal the organic enrichment mechanism. Results show that the samples are notably enriched in strontium, phosphorus and biogenic calcium (indicated by excess calcium concentrations) and reveal the mass death event of benthic organisms (including freshwater mussels and gastropods) in paleolakes under the control of climatic transformation. Such enrichment strongly supports the hypothesis that CaO is considered to be a paleoproductivity proxy to some extent. The paleolake was dominated by a warm and humid climate and rapid sedimentation rates and experienced intense chemical weathering, which are characteristic of freshwater input and a high flux of detrital fractions. The variations in the redox state and paleoproductivity are due to climatic shifts, hydrographic restrictions and biological behavior. Furthermore, the organic matter was enriched during both oxygenated and oxygen-deficient conditions. The combination of high sedimentation rates and high sinking influxes of particulate organic carbon reduced the chances of decomposition and thereby facilitated the efficiency of organic matter accumulation in an oxic environment. The low degree of organic matter degradation, moderate sedimentation rates and enhanced phosphorus recycling were responsible for the organic carbon accumulation and preservation in sediments for dysoxic bottom conditions.

1. Introduction

Organic matter (OM) enrichment mechanism in shale is a fundamental issue that guides shale oil and gas exploration. For organic-rich shale, the mechanisms of OM enrichment have largely focused on two aspects: productivity and preservation (Calvert and Pedersen, 1993; Arthur and Sageman, 1994). The productivity model highlights the sinking fluxes of organic carbon to the depositional interface as a result of high primary and export production (Caplan and Bustin, 1999). The preservation pattern suggests that dysoxic or anoxic bottom water hinders decomposition and thereby more OM is retained (Calvert and Pedersen, 1993; Sageman et al., 2003). Moreover, the detrital influx and sedimentation rates are likely to induce dilution of organic carbon in sediments but may improve preservation conditions to some extent (Ganeshram et al., 1999; Murphy et al., 2000; Tyson, 2001; Mansour et al., 2020). Some reports have mentioned that high organic carbon inventories exist in an oxygen-rich lacustrine basin under a shifting redox status due to aerobic OM remineralization based on the dissolved oxygen consumption (Liang et al., 2020; Xu et al., 2020). Consequently, the enrichment of OM should be considered the result of multiple factors, such as organic matter source and production, dilutive effect and preservation conditions. For shale with freshwater shell remains,

* Corresponding author. State Key Laboratory of Petroleum Resources and Prospecting, China University of Petroleum, Beijing, 102200, China.
E-mail address: lindachen@cup.edu.cn (D. Chen).

https://doi.org/10.1016/j.petrol.2022.111178
Received 20 March 2022; Received in revised form 11 October 2022; Accepted 28 October 2022
Available online 1 November 2022

benthic bivalves, as suspension-feeding invertebrates, have no effective contribution to paleoproductivity while the uptake of dissolved and particulate organic carbon sourced from phytoplankton, bacteria and debris by shellfish through filtration, ingestion, and absorption (Pan and Wang, 2004) may limit organic matter preservation. The significance of bivalve mollusks to organic carbon enrichment in sediments is poorly documented.

Information with respect to the elemental variations in the composition and concentration in sediments has been considered to provide data for the inversion and reconstruction of paleosedimentary environments (Floyd et al., 1990; Poulton and Canfield, 2011; Algeo and Ingall, 2007). Elements can be brought into sediments through biotic and abiotic actions (Algeo and Ingall, 2007). A close correspondence between the environmental conditions and elemental abundances has been established, such as for elements related to biogenesis (e.g., P, N and Ba), redox-sensitive trace elements (e.g., authigenic Mo, V, U, Co and Re), and elemental concentrations (e.g., Al, Ti, Zr, Ga and Rb) that are associated with terrigenous inputs fluxes and degrees of weathering, while Sr and B are correlated with salinity (Nesbitt and Young, 1982; Goodarzi and Swaine, 1994; Tribovillard et al., 2006; Ross and Bustin, 2009; Schoepfer et al., 2015; Wei and Algeo, 2020). Inorganic geochemical parameters are utilized to not only restore the paleoenvironment but also to determine the mechanisms of OM accumulation (Rimmer et al., 2004; Algeo and Lyons, 2006).

Freshwater mussels are a familiar constituent of the Da'anzhai lacustrine shale. Xu et al. (2017) considered that the Da'anzhai lacustrine shale formed in complex paleoenvironments with high terrestrial input and variable salinities. Liu et al. (2019) and Xiao et al. (2021) both reconstructed the paleoenvironment of the Da'anzhai lacustrine shale. They pointed out that the elevated primary productivity and oxygen-depleted preservation conditions were conducive to OM enrichment but ignored the influence of shell debris. Excessive enrichment in Sr in carbonate-rich formations due to the substitution of Sr^{2+} for Ca^{2+} influences the validity of elemental proxies such as Sr/Ba ratios (Wei and Algeo, 2020). Hence, the effect of calcareous bioclasts on the Sr contents must be assessed. Furthermore, the formation mechanism for

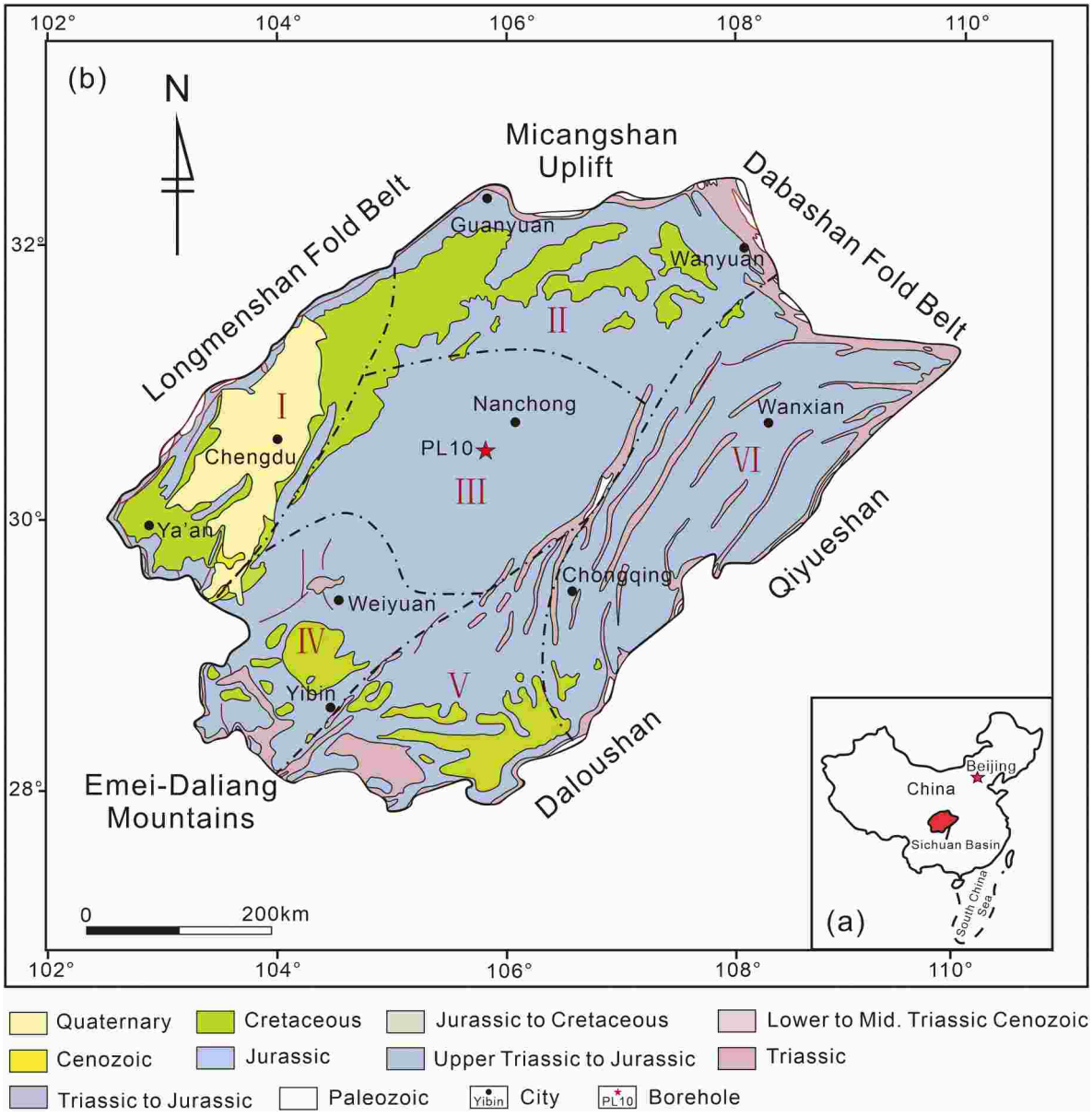

Fig. 1. Geological and tectonic map of the Sichuan Basin (modified from Liu et al., 2020). I: Western Sichuan Depression, II: northern gentle structural zone, III: central uplift, IV: southwestern gentle structural zone, V: southern gentle structural zone, and VI: eastern steep structural zone.

the organic-rich shale mixed with shell debris in the Da'anzhai Member fails to be fully revealed.

The Da'anzhai lacustrine shale provides favorable conditions for analyzing the controlling factors of OM enrichment and the geological significance of the shellfish contents for shale mixed with shell bioclasts employing inorganic geochemical indices. Because thermally mature shale or mudstone can retain abundant elemental information (Ross and Bustin, 2009), the Da'anzhai shale in the mature stage (e.g., Ro = 0.9–1.5%, referring to Yang et al., 2019) can be considered as an ideal target to establish sedimentary conditions.

In this study, the paleoenvironmental evaluation was performed by geochemistry. Moreover, an investigation of the mechanisms of OM enrichment for shell-rich lacustrine shale under variable conditions was conducted. These results will provide clarification for reconstructing the paleoenvironments of sediments that are mixed with shell remains by using elemental proxies and also provide a reference for the significance of biological shells in the OM enrichment of lacustrine shale.

2. Geological setting

The Sichuan Basin is located in the southwestern region of China and is composed of six tectonic belts, including the northern gentle structural zone, central uplift, southwestern gentle structural zone, southern gentle structural zone, Western Sichuan Depression, and eastern steep structural zone (Wang et al., 2021; Guo et al., 1996) (Fig. 1). The study area is situated in the central low flat zone of the Sichuan Basin, bounded by the Longquanshan fault belt in the east and Huayingshan fault in the west, and covers an area of approximately 40,000 km^2 (Xie et al., 2010).

From the Late Triassic to Late Jurassic, the northwestern margin of the Upper Yangtze Plate was inverted from a passive continental margin basin to a large and gentle foreland basin that was controlled by compression (Zheng et al., 2016). The basin was successively filled with terrigenous strata that consisted of the Upper Triassic Xujiahe Formation, Lower Jurassic Ziliujing Formation, Middle Jurassic Lianggaoshan and Shaximiao formations, Upper Jurassic Suining and Penglaizhen formations (Fig. 2a). Among these strata, the Da'anzhai Member of the Lower Jurassic Ziliujing Formation experienced a large-scale lacustrine transgression, during which a freshwater paleolake covered a wide area (Yang et al., 2019). From bottom to top, the Da'anzhai Member can be divided into three submembers: Da_3, Da_2 and Da_1 (Fig. 2b). The Da_3 submember was deposited with thick shell limestone interbedded with a few thin mudstone layers. The sediments in the Da_2 submember consist mainly of black calcareous mudstone and shale with high OM contents, which are regarded as having a great potential for shale oil. The Da_1 submember primarily consists of thick shell limestone and dark calcareous shale (Fig. 2b). The Da'anzhai Member can be identified as sedimentary sub-facies, including shallow lake and semi-deep lake. The Da_3 submember was shallow lacustrine sub-facies and further developed high-energy shelly beach microfacies. The semi-deep lacustrine facies was mainly developed in the Da_2 submember, which can be further subdivided into semi-deep lacustrine mud and storm gravity flows microfacies. Finally, the facies of the Da_1 submember was high-energy shelly beach microfacies which is similar to the Da_3 submember. The evolution of sedimentary facies indicates the variations of lake water from shallow to deep to shallow again.

3. Samples and analytical procedures

3.1. Samples

A total of 23 samples were used in this study and were collected from a lacustrine calcareous shale succession of the Da_2 submember from the

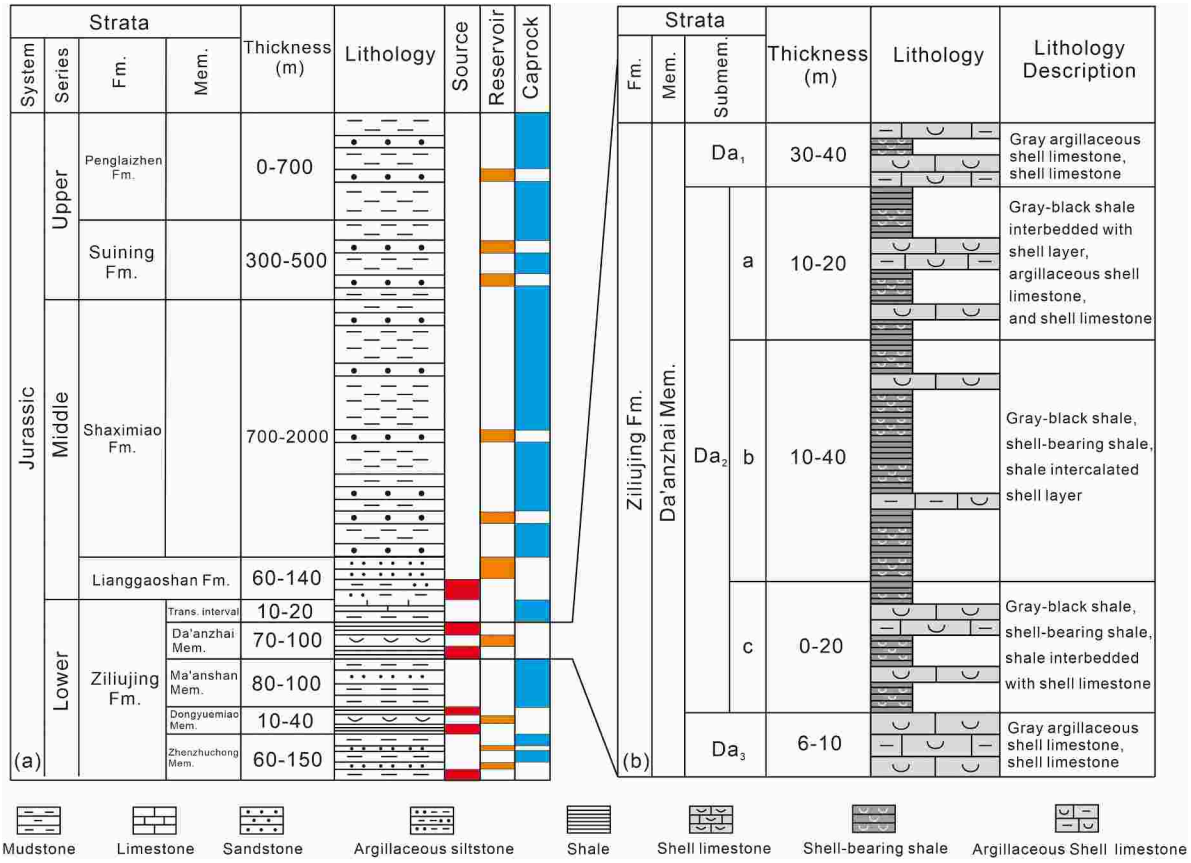

Fig. 2. (a) Jurassic stratigraphy of the central Sichuan Basin; (b) Stratigraphic column for the Da'anzhai Member. Fm. = Formation, Mem. = Member, Submem. = Submember, and Trans interval = Transition interval.

cored well PL10 in the central Sichuan Basin (Fig. 1). To reveal the geochemical characteristics of the entire sedimentary section, random sampling was conducted at intervals of 0.1–5 m to cover different lithologic types (Table 1). The samples obtained are 16 shell-bearing shales and 5 gray-black shales with only 2 shell limestone samples. In addition, each sample was broken into small parts according to the predetermined weights needed for different tests, and the total organic carbon (TOC) contents and major and trace elements were then determined separately.

3.2. TOC analysis

3.2.1. TOC testing

A total of 21 shale samples with shell-bearing shale and gray–black shale and 2 shell limestone samples were used for the TOC analysis. The TOC values of the powdered samples from the Da'anzhai lacustrine shales were measured at the Beijing Research Institute of Uranium Geology. The core samples were crushed and sieved with an 80 mesh sieve and then reacted with 10% HCl for 1 h to remove the inorganic carbon. Finally, the samples were placed in an oven at 60 °C to dry prior to analysis. The analytical instrument used was a CS580 carbon sulfur analyzer. Details are provided in GB/T 19145-2003 (the Chinese national standard), and the measurement precision was within 0.45%.

3.2.2. Method of the original TOC recovery

Based on the kerogen thermal degradation theory (Gersten et al., 2000), the model for source rock evolution and hydrocarbon generation and expulsion was proposed (Pang et al., 2014). Then according to material balance theory, the quantitative model of TOC variation in geological history was derived (Pang et al., 2014). The detailed derivation and calculation processes refer to Pang et al. (2014). The initial TOC recovery coefficient is calculated as follows:

$$K = \frac{TOC_O}{TOC} = \frac{1-\varphi_o}{1-\varphi} \bullet \frac{\rho}{\rho_o} \bullet \left(1 + R_p \bullet K_e \bullet K_C\right) \quad (1)$$

K is defined as the original TOC recovery coefficient. TOC_o is the original TOC content and TOC is the residual TOC measured in the laboratory at present. φ_o is the original porosity, and φ is present-day residual porosity. ρ_o is the original density and ρ represents the present-day density. R_p is the hydrocarbon generation ratio. K_e is hydrocarbon expulsion efficiency and K_c is the carbon-bearing coefficient of expulsed hydrocarbons. These parameters R_p, K_e and K_c are affected by kerogen type and thermal evolution degree. The values can be determined according to the charts established by Pang et al. (2014).

3.3. Elemental analysis

Geochemical analysis of the 23 core samples was carried out at the National Institute of Natural Hazards. First, the samples were crushed and ground to less than 200 mesh, then X-ray fluorescence spectroscopy (XRF) was used to identify the oxides of the major elements, including SiO_2, Al_2O_3, CaO, K_2O, Na_2O, Fe_2O_3, MnO, MgO, TiO_2 and P_2O_5. The analytical error was less than 5%, and the implementation method and standard is presented in GB/T 19145-2003 (the Chinese national standard). For the trace element analysis, all investigated samples were dissolved in 30% HF and 68% HNO_3 at 190 °C for 24 h. Subsequently, after evaporating the excess solvent at 130 °C for 3 h, the samples were redissolved in 2 mL of 6 mol/L HNO_3 in a capped Teflon tank at 150 °C for 48 h. In accordance with the experimental method and detection standard GB/T 14506.28-2010 (the Chinese national standard), inductively coupled plasma mass spectrometry (ICP-MS PE300D) was used to determine the trace elements. The test error was 0.1×10^{-12} to 9×10^{-12}.

Aluminum in sediments is limited to detrital aluminosilicate minerals (Calvert, 1976). Therefore, determining the concentrations of elements that represent non-terrestrial sources (e.g., biogenic calcium, silica and barium) to exclude detrital contributions is discussed. The nondetrital element contents were calculated by the formula:

$$Element_{xs} = element_{sample} - \left(Al_{sample} * (element/Al)_{PAAS}\right) \quad (2)$$

$Element_{xs}$ is defined as the element level above the Post Archean Australia Shales (PAAS) (Taylor and Mclennan, 1985), which means a non-terrestrial origin. $Element_{sample}$ represents the total concentration of the target elements. $(element/Al)_{PAAS}$ is the ratio of the investigated element to Al in PAAS.

The element enrichment factors ($Element_{EF}$), which are the element contents normalized by Al, were compared to those of the PAAS background. The EFs were determined using formula 3 (Ross and Bustin, 2009):

Table 1
TOC (wt.%), Ro (%), original TOC recovery coefficient K, and the original TOC values (wt.%) of 23 samples from the Da'anzhai Member.

Sample No.	Depth (m)	Lithology	TOC (%)	Ro (%)	K	TOC_o (%)	Sample No.	Depth (m)	Lithology	TOC (%)	Ro (%)	K	TOC_o (%)
PL10-6	2031.6	Shell-bearing shale	0.99	1.04	1.2	1.19	PL10-27	2007.8	Shell-bearing shale	1.38	1.04	1.2	1.66
PL10-7	2029.8	Shell-bearing shale	0.6	1.04	1.2	0.72	PL10-30	2002.2	Shell-bearing shale	0.9	1.04	1.2	1.08
PL10-9	2027.5	Gray-black shale	0.69	1.04	1.2	0.83	PL10-32	1998.6	Gray-black shale	1.61	1.04	1.2	1.93
PL10-10	2026.7	Shell-bearing shale	0.86	1.04	1.2	1.03	PL10-33	1998.5	Shell-bearing shale	0.72	1.04	1.2	0.86
PL10-12	2022.7	Shell-bearing shale	0.73	1.04	1.2	0.88	PL10-36	1995.3	Shell-bearing shale	2.4	1.03	1.2	2.88
PL10-13	2022.2	Gray-black shale	0.71	1.04	1.2	0.85	PL10-37	1993.4	Gray-black shale	1.07	1.03	1.2	1.28
PL10-14	2021.1	Shell limestone	0.69	1.04	1.2	0.83	PL10-40	1989.8	Shell-bearing shale	0.94	1.03	1.2	1.13
PL10-17	2019.1	Shell-bearing shale	1.41	1.04	1.2	1.69	PL10-43	1985.0	Shell-bearing shale	0.58	1.03	1.2	0.70
PL10-19	2016.4	Shell-bearing shale	0.89	1.04	1.2	1.07	PL10-45	1983.1	Shell-bearing shale	1.6	1.03	1.2	1.92
PL10-20	2015.2	Shell-bearing shale	1.14	1.04	1.2	1.37	PL10-48	1979.2	Shell limestone	0.35	1.03	1.2	0.42
PL10-22	2014.3	Gray-black shale	2.9	1.04	1.2	3.48	PL10-50	1978.1	Shell-bearing shale	0.32	1.03	1.2	0.38
PL10-24	2011.8	Shell-bearing shale	1.82	1.04	1.2	2.18	–	–	–	–	–	–	–

Note: K is the original TOC recovery coefficient, and TOC_o is the original TOC value.

$$Element_{EF} = (element/Al)_{sample} \Big/ (element/Al)_{PAAS} \quad (3)$$

where $(element/Al)_{sample}$ is the ratio of the elemental concentrations to Al in shale samples. EFs >3 mean that the elemental enrichment degree exceeds the average crustal values, and EFs >10 can be considered to indicate moderate to intense enrichment of the investigated element (Algeo and Tribovillard, 2009).

The mineral and chemical compositions of the sediments that are derived from provenances can effectively reflect the degree of weathering. Therefore, the chemical index of alteration (CIA) can be used as a quantitative index to analyze climate change; that is, the CIA values of sediments in hot and humid climates are higher, whereas the CIA values are lower in cold and arid climates (Nesbitt and Young, 1982). The CIA values can be calculated by the following formula and the molar proportions of each oxide were used:

$$CIA = Al_2O_3 / [(Al_2O_3 + CaO^* + Na_2O + K_2O)] \times 100 \quad (4)$$

where CaO* represents the CaO content that is derived solely from the silicate fraction. If the remaining CaO > Na_2O in molar proportions, the CaO* is considered to be equal to Na_2O; otherwise, CaO* is equivalent to the remaining CaO. Generally, the CIA values range from 85 to 100 which indicate hot and humid climates, and in clusters between 70 and 85, which indicate warm and humid climates. In addition, the CIA values of sediments deposited in cold and arid climates range from 50 to 70 (Nesbitt and Young, 1982; Fedo et al., 1995).

4. Results

4.1. Lithology properties

According to observations of cores and thin sections of the shale samples from well LP10, the Da'anzhai lacustrine shale strata are characterized by gray–black shale, shell-bearing shale and shell limestone (Fig. 3a, b, c). The shell layers formed due to the massive development of shells and sedimentation of shell debris with mud (Kidwell, 1991) (Fig. 3b, h), which represent interlayer or interbedded shale. Furthermore, the shell debris mixing in shale strata usually increases the carbonate content of samples, for example, PL10-14, PL10-17, PL10-27 and PL10-36 (Fig. 3e–h). Therefore, the Da'anzhai shale is a typical calcareous shale. Microscopic and core petrological characteristics show that these samples still belong to shell-bearing shale (Fig. 3b, f, g, h).

4.2. Present-day and original total organic carbon content

The results of the TOC testing are shown in Table 1. The total organic carbon contents of the Da'anzhai lacustrine calcareous shale range from 0.32% to 2.9%, with an average of 1.1%. Similar results were obtained by Xu et al. (2017). The TOC contents of the shale in the Jurassic Da'anzhai Member vary widely and have some higher values that are over 2%. Through a statistical analysis of the TOC results, it was found that the samples with TOCs greater than 1% accounted for only 39%, of which only 2 samples (PL10-22, PL10-36) were greater than 2%. The TOCs remain stable at low levels (<1.0%) and suddenly increases to 2.9% at 2014.3 m. Subsequently, the TOCs slowly decrease and then increase to 2.4% at 1995.3 m. Finally, these concentrations gradually drop to low levels at the top of the Da_2 submember (Table 1, Fig. 6).

The shale maturity index (Ro) and kerogen types were determined before the original TOC was restored. Yang et al. (2019) reported that the relationship between Ro and depth and the Da'anzhai lacustrine shale is dominated by type II organic matter. The original TOC recovery coefficient chart for muddy hydrocarbon source rocks of different kerogen types was established by Pang et al. (2014). Here, according to organic matter type and thermal maturity of the Da'anzhai shale, the recovery coefficient K and the original TOC were obtained (Table 1). The result shows that the recovery coefficient K is about 1.2 and the TOC_o contents have a range from 0.12% to 3.48% and an average of 1.24%. Due to TOC_o having a linear relationship with TOC, the peak value and variation trend of TOC_o are consistent with TOC. Furthermore, the restored original TOC_o was used in the whole discussion of this manuscript and the redox indicator Corg:P values were calculated by TOC_os.

4.3. Elemental geochemistry

4.3.1. Distribution of major elements

The variations in the major element compositions of the lacustrine calcareous shale samples are presented in Table 2. SiO_2 is the dominant component in the studied Da'anzhai shale samples relative to Al_2O_3 and CaO, with an average of 48.48% and a range from 7.52% to 59.35%. The shale samples examined have an average Al_2O_3 concentration of 17.21% and range between 2.03% and 22.35%, while the CaO contents average 11.99% and range from 1.33% to 66.44%. The three secondary oxides, including K_2O, Fe_2O_3 and MgO, are present with averages of 2.85%, 6.13% and 2.24%, respectively. MnO, Na_2O, P_2O_5, and TiO_2 exhibit mean values of 0.07%, 0.49%, 0.24% and 0.65%, respectively. Moreover, the excess calcium and silica are obtained by Equation (2). Ca_{xs} has a wide range between 0.21% and 52.99%, with an average of 11.90%. The Si_{xs} concentrations in the Da'anzhai shales are all negative, and the EFs are <1 (Table 2, Fig. 4).

Notable enrichments of Ca and P are observed in each lithology (Fig. 4). The high Ca contents are closely related to the abundant residual brachiopods and bivalve fossils in the shale strata, as evidenced by a strong negative correlation with Al and extremely high EF values (Appendix Table A1, Fig. 4). The excess Ca obtained by Eq. (2) is used to characterize biogenic Ca (Table 2). The magnesium in the Da'anzhai sediments is mainly associated with dolomite. The EF value for phosphorus is greater than 1 in all lithology types, which is a result of authigenic enrichment due to the circulation of nutrient elements in organisms (e.g., algae and plankton) (Redfield, 1958; Tyrrell, 1999). Notably, both Ca, Mn and P are highly enriched in shell limestone, which may imply that much of the shell debris and algae were buried and preserved in the shallow region. Furthermore, a similar condition can also be observed in other lithologies, but at a lower degree of enrichment (Fig. 4). The Na concentrations may reflect the abundance of plagioclase. The K contents are mostly related to illite and K-feldspar in the shale samples. The higher EFs of K than those of Na for the Da'anzhai shales with lower K-feldspar contents suggest that plagioclase dominates over K-feldspar, but a large amount of K is attributed to clay minerals. Titanium, a stable element in sediments during diagenesis, has EFs<1. The weak correlation between Ti and Al ($r = 0.47$) is due to that Ti may not only be terrestrially sourced but enriched authigenically (Appendix Table A1) (Chaikovskiy et al., 2019).

4.3.2. Distribution of trace elements

The trace element concentrations in the samples from the Da'anzhai lacustrine calcareous shales in the present study are shown in Table 3. The most enriched trace element is Sr, with a range between 166.72 ppm and 1004.00 ppm and an average of 341.5 ppm (Table 3), which is likely to be adsorbed by carbonate (Fig. 5) (Wei and Algeo, 2020). The abundant Sr levels in the three lithologies are consistent with the characteristics of the broad development of shellfish (Fig. 3 e, g, h). In addition, the degrees of enrichment of certain elements, including V, Cr, Ga, Rb, Ba, La, Yb, Pb, Th and U, bear a resemblance to those of PAAS in the gray-black shales and shell-bearing shales, with EFs of approximately 1 (Fig. 5). Compared with the other two lithologies, Ni, Ba and Pb are relatively enriched in shell limestone. The relatively high enrichment of Ba could indicate shell debris and algae a symbiotic relationship between shells and algae in the lake. These elements (Zr, Nb, Hf and Ta) are characterized by relatively high depletions (Fig. 5). However, Mo as a typical redox-sensitive element has not been detected in this study.

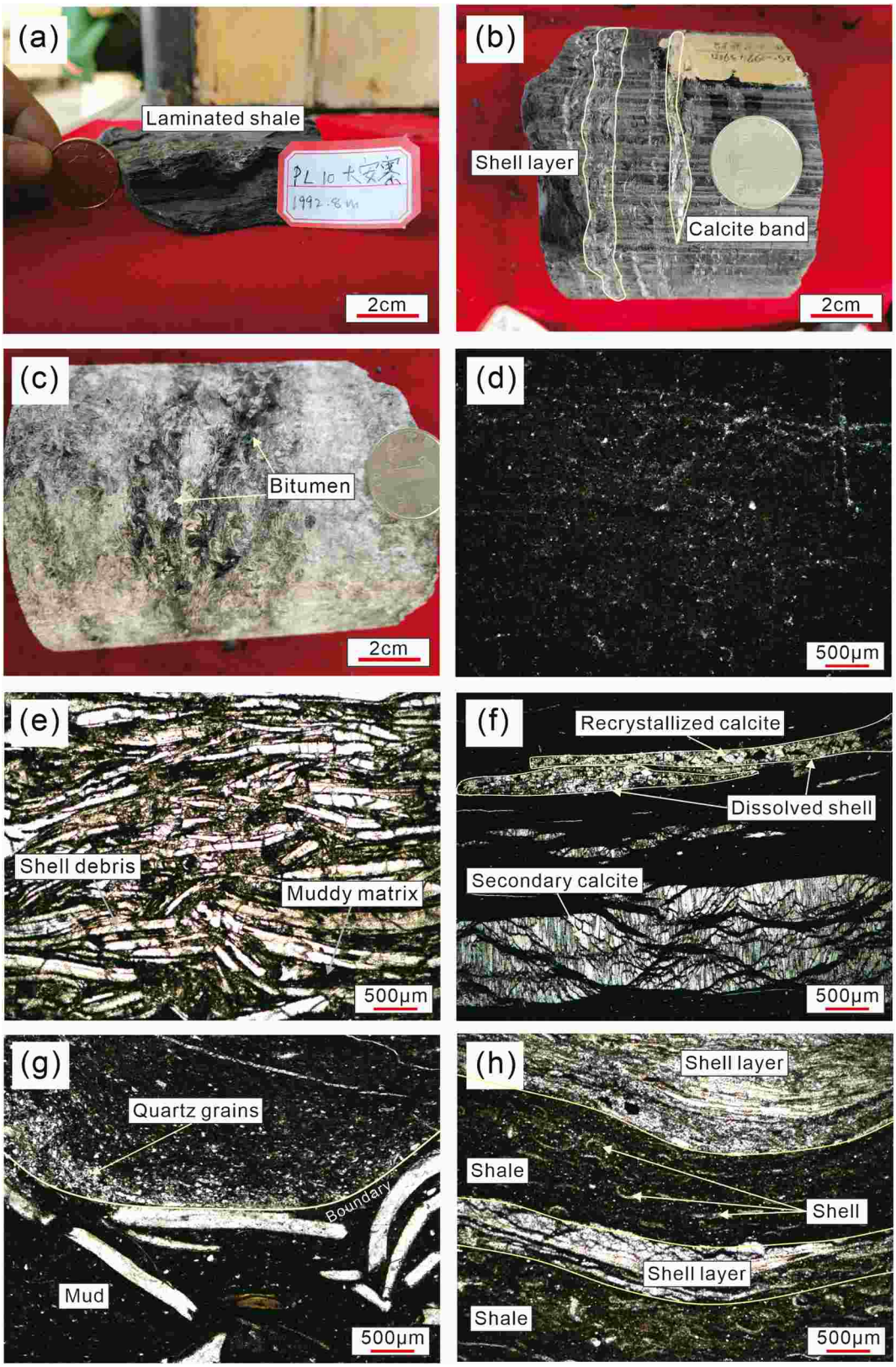

Fig. 3. Core and photomicrographs showing the representative lithologic characteristics of the Da'anzhai lacustrine shale. (a) Typical black laminated shale, 1992.8 m, Well PL10; (b) Gray–black shale intercalated shell layers and a few calcite bands, 1994.25–1994.39 m, Well PL10; (c) Gray massive shell limestone and oil immersion, the residual pores between the biological shell are filled with bitumen, 1981.57–1981.78 m, Well PL10; (d) Dark gray shale with no biological shells, single polarized light, 25 × , PL10-30; (e) Broken shells are stacked and the interspaces are filled with a muddy matrix, single polarized light, 25 × , PL10-14; (f) Black shale, with calcite recrystallized in the dissolved pores of the shell detritus, single polarized light, 25 × , PL10-36; (g) Accumulation of quartz grains within the shale matrix caused by debris flow, and the boundary between detrital silica and mud, single polarized light, 50 × , PL10-7; and (h) Shell layers and shale are interbedded, and small shells are arranged horizontally in shale, single polarized light, 25 × , PL10-17.

Table 2
Major element concentrations in the Da'anzhai lacustrine shale from the well PL10 samples (wt.%).

Sample No.	Lithology	Depth	Al_2O_3	CaO	Fe_2O_3	K_2O	MgO	MnO	Na_2O	P_2O_5	SiO_2	TiO_2	Ca_{xs}	Si_{xs}
		m	%	%	%	%	%	%	%	%	%	%	%	%
PL10-6	Shell-bearing shale	2031.6	15.67	18.69	5.03	2.43	1.83	0.07	0.42	0.30	41.69	0.60	12.80	−4.84
PL10-7	Shell-bearing shale	2029.8	17.54	7.01	8.51	2.61	2.20	0.17	0.44	0.17	50.45	0.65	4.41	−3.65
PL10-9	Gray-black shale	2027.5	18.33	3.71	6.96	2.53	2.19	0.16	0.45	0.22	57.08	0.80	1.91	−1.78
PL10-10	Shell-bearing shale	2026.7	16.78	8.04	5.18	2.42	1.96	0.06	0.42	0.44	53.65	0.86	4.95	−0.97
PL10-12	Shell-bearing shale	2022.7	19.46	3.08	5.80	2.95	2.07	0.05	0.47	0.13	52.61	0.73	1.53	−5.61
PL10-13	Gray-black shale	2022.2	15.63	19.54	6.40	2.26	1.83	0.11	0.44	0.46	46.15	0.71	13.30	−2.69
PL10-14	Shell limestone	2021.1	2.03	66.44	2.78	0.22	0.65	0.12	0.10	0.41	7.52	0.08	47.38	0.36
PL10-17	Shell-bearing shale	2019.1	19.50	3.68	6.76	3.13	2.03	0.04	0.51	0.14	55.91	0.86	1.84	−4.14
PL10-19	Shell-bearing shale	2016.4	16.51	7.61	6.37	2.49	1.80	0.07	0.55	0.21	54.55	0.82	4.68	−0.14
PL10-20	Shell-bearing shale	2015.2	20.34	1.44	6.67	3.19	2.05	0.05	0.57	0.19	59.27	0.89	0.21	−3.87
PL10-22	Gray-black shale	2014.3	20.05	2.29	7.40	3.21	2.12	0.04	0.54	0.15	56.06	0.73	0.96	−4.92
PL10-24	Shell-bearing shale	2011.8	19.47	3.47	6.60	3.12	2.17	0.04	0.56	0.21	56.16	0.79	1.75	−3.97
PL10-27	Shell-bearing shale	2007.8	19.92	3.78	6.58	3.15	2.38	0.04	0.65	0.08	55.35	0.77	1.99	−5.05
PL10-30	Shell-bearing shale	2002.2	19.24	2.26	6.23	3.31	2.54	0.02	0.65	0.11	59.35	0.64	1.03	−2.13
PL10-32	Gray-black shale	1998.6	21.21	1.33	6.12	3.93	2.81	0.03	0.71	0.16	56.97	0.66	0.34	−6.29
PL10-33	Shell-bearing shale	1998.5	15.46	11.11	5.69	2.91	2.43	0.03	0.56	0.08	46.46	0.50	7.48	−2.28
PL10-36	Shell-bearing shale	1995.3	11.79	28.67	4.70	2.29	3.03	0.06	0.43	1.17	32.91	0.45	20.06	−2.92
PL10-37	Gray-black shale	1993.4	19.88	4.87	6.55	3.73	2.93	0.03	0.67	0.15	52.99	0.62	2.91	−6.09
PL10-40	Shell-bearing shale	1989.8	22.35	1.65	7.66	3.88	2.74	0.04	0.50	0.11	54.61	0.72	0.52	−9.16
PL10-43	Shell-bearing shale	1985.0	21.14	3.66	7.59	4.07	2.94	0.05	0.48	0.17	51.83	0.71	1.96	−8.58
PL10-45	Shell-bearing shale	1983.1	20.70	1.54	5.96	3.64	2.68	0.02	0.56	0.12	58.14	0.75	0.41	−4.96
PL10-48	Shell limestone	1979.2	3.73	62.65	2.75	0.64	1.53	0.16	0.14	0.26	8.59	0.12	44.64	−1.77
PL10-50	Gray-black shale	1978.1	19.13	9.33	6.66	3.47	2.60	0.06	0.41	0.15	46.64	0.60	6.11	−7.89

Note: "/" means no data. The elemental concentrations of the Post Archean Australia Shales (PAAS) are derived from Taylor and Mclennan (1985).

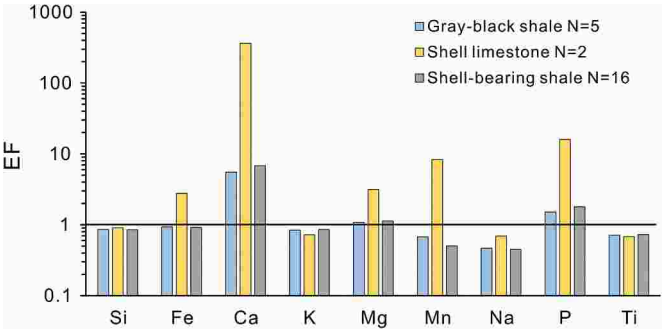

Fig. 4. Averages of the enrichment factors of the major elements relative to the Post Archean Australia Shales (PAAS) for different lithology (Taylor and Mclennan, 1985). The horizontal line with EF = 1 is used to highlight the enrichments or depletions of elements.

5. Discussion

5.1. Differences in organic matter accumulations

The organic carbon contents in shales vary with the sedimentary environments (Sageman et al., 2003; Rimmer et al., 2004). The organic-rich shale of the Da'anzhai Member at the ~1994 m–2000 m stratigraphic level with TOC_o up to 2.88%, is characteristic of bioclasts mixed in sediments (Fig. 6). The lithology for this interval is dominated by shell-bearing shale (Fig. 3f). Moreover, the shale at depths from 2010 m to 2016 m is enriched in OM, and the maximum TOC_o values reach 3.48%. However, the lithology for this shale section is different from that of the former shale, which is mainly gray–black shale without shellfish debris (Fig. 3d). In contrast, the organic material is enriched in diverse lithologic sections, which reveals the mechanism of OM accumulations in different environments. Furthermore, the OM in the sediments is relatively low for the remaining strata, with an average TOC_o of 1.02% (Fig. 6).

Generally, there are obvious differences in OM enrichment in the Da'anzhai shale, and the two shale sections contain high amounts of organic carbon under their unique sedimentary conditions.

5.2. Paleoenvironment associated geochemical records

5.2.1. Paleoclimate

Paleoclimate affects water level changes and water environmental conditions. The paleotemperature, humidity and sunshine amount control the species diversity, biomass and deposition of carbonates (Nesbitt et al., 1996). Furthermore, warm climatic conditions tend to provide adequate rainfall, which allows rivers to transport nutrients and OM to lakes, which further increases the primary productivity (Murphy et al., 2000). However, a warm climate can also result in stratification, weak flow circulation, and high oxygen levels in surface water. Shells are abundant in the Da'anzhai shale deposits and record the paleotemperature and paleosalinity information. The shales in the present study are in the mature evolution stage, which is an excellent subject for reconstructing the paleoenvironment.

In this study, the CIA values are utilized to reconstruct the paleoclimates during the deposition of the Da'anzhai shale. Due to Goodarzi and Gentzis (2018) discouraging the use of the CIA for samples with >30% of carbonate content without a pre-treatment, 7 samples with high carbonate recognized under the microscope were not calculated (PL10-6, PL10-12, PL10-14, PL10-17, PL10-27, PL10-36, and PL10-48). The calculations for the CIA values are listed in Table 4. The CIA values of the Da'anzhai shale vary from 75.59 to 81.29, with an average of 78.61, which indicates a reasonable association with warm and humid climatic conditions (Fig. 6). Although the CIA values fall within the range of warm and humid climates, there are still some fluctuations within a narrow range, which imply variations in temperature and precipitation. From the bottom to the top, the CIA value decreases first and then increases, and reaches the minimum value near 1992–2000 m. The decreasing values correspond to shell limestones or shell layers in shale and indicate that relatively cold and arid climatic conditions resulted in low recharge levels by streams due to sparse rainfall (Fig. 6). Such changes in climatic conditions will lead to increased ecological stresses on aquatic organisms, resulting in massive deaths of benthic freshwater shell organisms, which thereby provide a foundation for the deposition of carbonates in turbulent clear environments, as is evidenced by the intense enrichment in P and Ca in the same period. Subsequently, the climate transitioned toward a stable warm-humid period (Fig. 6).

Table 3
Trace element concentrations in the Da'anzhai lacustrine shale from the well PL10 samples (ppm).

Sample No.	Lithology	Depth (m)	V	Cr	Co	Ni	Cu	Ga	Rb	Sr	Zr	Nb	Ba	La	Yb	Hf	Ta	Pb	Th	U	Ba_{xs}
PL10-6	Shell-bearing shale	2031.6	122.14	91.16	10.70	32.74	36.80	19.12	124.00	230.00	105.12	9.68	525.60	25.28	2.01	2.79	0.60	9.77	10.75	1.82	−13.09
PL10-7	Shell-bearing shale	2029.8	108.98	109.36	13.11	41.14	33.64	20.86	147.76	243.80	137.88	10.61	489.80	33.08	2.73	3.50	0.76	18.63	17.29	2.50	−113.18
PL10-9	Gray-black shale	2027.5	122.40	101.90	15.51	44.04	38.56	21.44	152.82	187.44	151.02	13.12	443.00	42.8	3.32	3.92	0.96	24.62	20.30	3.37	−187.14
PL10-10	Shell-bearing shale	2026.7	111.30	112.04	15.52	43.00	40.64	20.16	127.28	252.00	181.32	14.47	449.00	48.46	3.70	4.52	1.08	22.10	22.16	3.19	−127.85
PL10-12	Shell-bearing shale	2022.7	112.62	84.42	11.96	36.38	31.62	16.78	110.64	404.20	109.98	11.10	534.80	25.66	2.22	3.13	0.65	15.80	10.77	2.04	−134.18
PL10-13	Gray-black shale	2022.2	73.66	120.74	17.95	52.52	40.56	24.62	177.72	179.66	158.84	13.52	643.80	36.34	2.87	3.93	0.91	20.22	18.56	2.59	106.48
PL10-14	Shell limestone	2021.1	12.69	9.57	2.33	8.88	6.92	1.80	8.82	1004.00	13.89	0.94	230.60	4.904	0.42	0.35	0.06	2.96	1.34	0.39	160.81
PL10-17	Shell-bearing shale	2019.1	115.88	109.42	18.27	49.20	43.74	23.40	168.06	196.70	175.94	15.00	647.80	30.74	2.68	4.32	0.96	23.00	16.56	3.03	−22.56
PL10-19	Shell-bearing shale	2016.4	131.00	97.90	15.43	42.16	40.12	19.40	117.28	321.00	161.36	13.47	534.00	36.68	2.79	4.14	0.89	25.22	17.43	2.76	−33.57
PL10-20	Shell-bearing shale	2015.2	73.14	120.58	19.17	53.34	46.02	24.98	182.66	181.86	187.26	15.62	667.80	40.66	3.40	4.64	1.09	27.14	21.44	3.14	−31.44
PL10-22	Gray-black shale	2014.3	173.30	105.38	16.96	49.82	42.44	23.52	176.80	166.72	140.68	12.86	659.60	24.28	2.14	3.56	0.83	19.68	12.24	3.00	−29.67
PL10-24	Shell-bearing shale	2011.8	93.84	123.46	16.53	52.08	48.40	24.22	177.68	233.40	159.68	14.07	668.20	36	3.08	4.05	0.97	22.12	18.73	3.25	−1.13
PL10-27	Shell-bearing shale	2007.8	199.60	111.70	17.17	46.66	42.38	23.70	164.76	237.00	150.30	12.30	679.00	23.54	2.23	3.81	0.81	18.50	12.76	3.12	−5.80
PL10-30	Shell-bearing shale	2002.2	114.08	110.56	13.92	46.36	41.52	23.72	175.98	226.00	135.36	10.63	643.00	29.42	2.47	3.43	0.71	14.98	15.01	2.59	−18.42
PL10-32	Gray-black shale	1998.6	218.60	124.10	15.83	45.80	46.06	25.62	197.60	212.00	125.08	10.74	751.60	26.22	2.22	3.21	0.74	13.93	13.35	3.73	22.46
PL10-33	Shell-bearing shale	1998.5	140.08	91.02	13.11	45.12	33.74	19.39	120.68	552.80	95.76	7.79	625.60	18.818	1.67	2.50	0.53	14.59	9.11	2.21	94.13
PL10-36	Shell-bearing shale	1995.3	109.10	61.82	8.51	27.44	25.92	13.22	94.10	610.80	66.14	5.69	432.40	23.84	1.67	1.85	0.38	10.33	6.82	3.41	27.09
PL10-37	Gray-black shale	1993.4	214.40	125.48	15.80	48.08	50.96	25.54	195.24	386.20	121.10	10.14	758.40	26.12	2.31	3.13	0.67	14.14	11.78	2.71	74.98
PL10-40	Shell-bearing shale	1989.8	197.64	126.34	19.05	54.36	46.62	26.94	197.78	205.60	135.88	11.27	700.00	29.82	2.41	3.49	0.75	17.91	17.43	2.66	−68.33
PL10-43	Shell-bearing shale	1985	114.34	110.14	13.98	38.84	25.94	18.65	197.82	196.90	115.34	9.03	531.80	42.36	2.75	3.02	0.64	17.32	20.24	2.44	−194.94
PL10-45	Shell-bearing shale	1983.1	188.64	119.38	13.89	49.58	42.46	25.36	197.00	238.80	142.18	12.42	735.60	32.04	2.58	3.60	0.83	18.00	18.28	2.86	23.99
PL10-48	Shell limestone	1979.2	21.16	15.73	4.32	11.14	8.44	3.55	22.62	665.60	16.73	1.43	152.00	5.636	0.45	0.46	0.08	4.26	2.22	0.56	23.77
PL10-50	Gray-black shale	1978.1	135.30	107.66	15.75	45.46	33.16	23.12	172.96	234.60	115.68	10.20	496.60	37.62	2.35	3.02	0.74	25.44	17.37	2.63	−161.04
PAAS*	/	/	150	110	23	55	50	20	160	200	210	18	650	38.2	2.82	5	1.28	20	14.6	3.10	−13.09

Note: "/" means no data. The elemental concentrations of the Post Archean Australia Shales (PAAS) are derived from Taylor and Mclennan (1985).

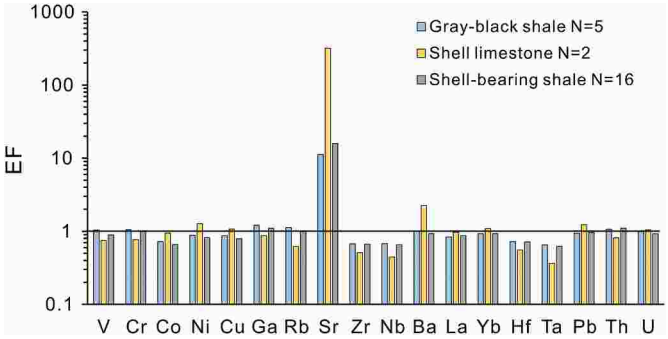

Fig. 5. Averages of the enrichment factors of trace elements relative to the Post Archean Australia Shales (PAAS) for different lithology (Taylor and Mclennan, 1985). The horizontal line with EF = 1 is used to highlight the enrichments or depletions of elements.

In addition, fluctuations in the contents of Al, K, Rb and Ga have been recorded for climate changes. Ga/Rb and K_2O/Al_2O_3 ratios as a geochemical proxy are useful to climatic records (Roy and Roser, 2013). Kaolinite in humid and warm climates is enriched in Al and Ga, which are usually associated with fine-grained aluminosilicate fractions (Hieronymus et al., 2001; Beckmann et al., 2005). K and Rb are related to illite, indicating weak chemical weathering and cool and dry climatic conditions (Ratcliffe et al., 2010). Therefore, sediments rich in illite have low Ga/Rb and high K_2O/Al_2O_3 ratios, whereas those rich in kaolinite have high Ga/Rb and low K_2O/Al_2O_3 ratios. For the Da'anzhai calcareous shale, the Ga/Rb and K_2O/Al_2O_3 ratios range from 0.09 to 0.2 and from 0.11 to 0.19 respectively, both showing low values. Shale sample points are concentrated between warm/wet and cool/dry climates, as evidenced by an abundance of illite (6.10–51.16%, average 25.11%, referring to Xu et al., 2017), and moderate weathering associated with appropriate warm/wet climatic conditions and a small amount of kaolinite (1.22–8.25%, average 4.80%, referring to Xu et al., 2017) formed in intense chemical weathering under warm/wet climates (Fig. 7) (El Mourabet et al., 2018.). These results indicate a relatively warm and humid climate with both dry and wet periods.

5.2.2. Origin of silica and terrigenous detrital input

The origins of silica include chemical, biological, volcanic and hydrothermal processes (Calvert, 1974). Si is usually associated with siliciclastic and biological compositions. In this study, the Si_{EF} is 0.85 less than 1 (Fig. 4) with no excess silica ($Si_{xs} < 0$ for all samples) (Table 2), and Si values exhibit a strong positive correlation with Al (Fig. 8a), which provides strong evidence that although the Si contents were depleted relative to those of PAAS, a nondetrital source of silica can be completely discounted for the Da'anzhai shales. The presence of detrital silica can be proven through observations of the accumulations of quartz grains within an argillaceous matrix, which are identified by the characteristics of the boundary between sands and muds caused by debris flows (Fig. 3g). Aluminum concentrations in sediment are related to clay fractions and are controlled by the detrital input dynamic to some extent. However, the Al content of the Da'anzhai shales is signally negatively correlated with CaO, which influences the validity of it as an indicator of terrigenous input. Although Al/Si ratio shows a narrow variation, it has a similar variation trend to terrigenous Si (Fig. 6). Therefore, the Al/Si ratio was used to estimate detrital influxes.

The levels of the high field strength elements (e.g., Zr, Hf, Nb, Ga, Ta and Th) are mainly controlled by the aluminosilicate compositions (Plank and Langmuir, 1998; Murphy et al., 2000). Zr, Hf, Nb, Ta and Th are not correlated with Al_2O_3 and have enrichment factors below 1 (Appendix Table A1; Fig. 5). Ga is chosen as a diagenetic immobile element because 1) Ga_{EF} is close to 1, which is consistent with the PAAS (Fig. 5); and 2) Ga exhibits a good correlation with Al_2O_3 (Fig. 8b). Furthermore, the majority of Ga is derived from river input due to the weathering of silicate rock (McAlister and Orians, 2015). Most dissolved Ga is likely to precipitate in sediments before entering lakes because of its low solubility (Shiller and Frilot, 1996). These factors indicate that Ga records most of the provenance information and low biogenetic dilution of Ga during deposition. Moreover, Fe + K values are a practical proxy to assess detrital input influxes (Arthur and Dean, 1998).

In this study, silica in the Da'anzhai shales is proven to originate as siliciclastics (quartz). Therefore, Si, Al/Si, Ga and Fe + K can be considered as indicators of terrigenous detrital input influxes. These investigated proxies show similar trends, which reveal high levels of land-derived clasts from a consistent source (Fig. 6). In the Da_2 submember, for well PL10, the detrital input influxes remain stable and high, and only several large variations occur because of paleoclimate transitions (Fig. 6). This is due to open and freshwater lacustrine depositions with a stable rate of discharge to recharge, possibly indicative of the constant fluvial contributions to recharge (Fig. 3a, d) (Wang et al., 2006). In lacustrine sedimentary systems, the sediment and plant debris that are formed by intense chemical weathering are injected into the basin by surface runoff, which usually occurs in warm-humid climates with heavy rainfall (Nesbitt et al., 1996). The pronounced correspondence between the inputs of terrigenous debris and the paleoclimate parameters confirms that a warm-humid climate was accompanied by high influxes of terrestrial inputs, while a relatively cold-arid climate resulted in a low influx of detrital fractions for the Da'anzhai shale (Fig. 6).

5.2.3. Paleowater condition

The characteristics of lacustrine calcareous shale vary when compared to those of marine shale due to the complex and different sedimentary paleoenvironments (Bohacs et al., 2000). The paleowater conditions mainly include paleosalinity and paleoredox conditions, which affect the accumulation and preservation of OM (Tyson and Pearson, 1991; Poulton and Canfield, 2011). Investigating trace elements is effective for providing an understanding of the paleowater characteristics. In the present study, the self-stable elements (e.g., Sr, Ba, V, Ni, Co, Th, K and Cr) and trace element ratios are used to analyze the paleosalinity and paleoredox conditions during the Da'anzhai sedimentary period (Calvert and Pedersen, 1993; Jones and Manning, 1994).

5.2.3.1. Paleosalinity. Various geochemical proxies have been used in paleosalinity analyses, which mainly include the B/Ga, Sr/Ba and S/TOC ratios of ancient sediments (Wei and Algeo, 2020). However, the B and S concentrations have not been measured in the Da'anzhai calcareous shale. Furthermore, it is recommended that screening for biogenic Ba in all paleosalinity studies make use of Sr/Ba ratios (Wei and Algeo, 2020). Excess (biogenic) Ba can potentially shift bulk-sediment Sr/Ba to lower values than present in the clay fraction, resulting in incorrect paleosalinity interpretations (Wei and Algeo, 2020). In the present study, the calculated excess Ba obtained by Equation (2) are commonly negative and we found no examples with obvious biogenic Ba influence (Table 3). Hence, in the present study, the Sr/Ba ratios was selected as an indicator to evaluate the paleosalinity levels.

Riverine input provides the major contribution to the large amounts of Sr that are released into lakes due to chemical weathering processes, and dissolved Sr^{2+} tends to precipitate under high-salinity conditions (Godderis and Veizer, 2000; Ding et al., 2001). Because Sr^{2+} substitutes easily for Ca^{2+} in carbonate due to its ionic radius that is similar to that of Ca^{2+}, anomalous enrichment of Sr forms a series of compounds, including $SrSO_4$ and $SrCO_3$ (Roden et al., 2002), which means that calcareous bioclasts mixed with shale are potentially likely to increase the Sr/Ba ratios. Thus, considering the development of lacustrine coquina and intense Sr enrichment in the Da'anzhai lacustrine sediments (Fig. 5), one critical treatment of calibration of carbonate-hosted Sr contents should be conducted. The calibration method proposed by

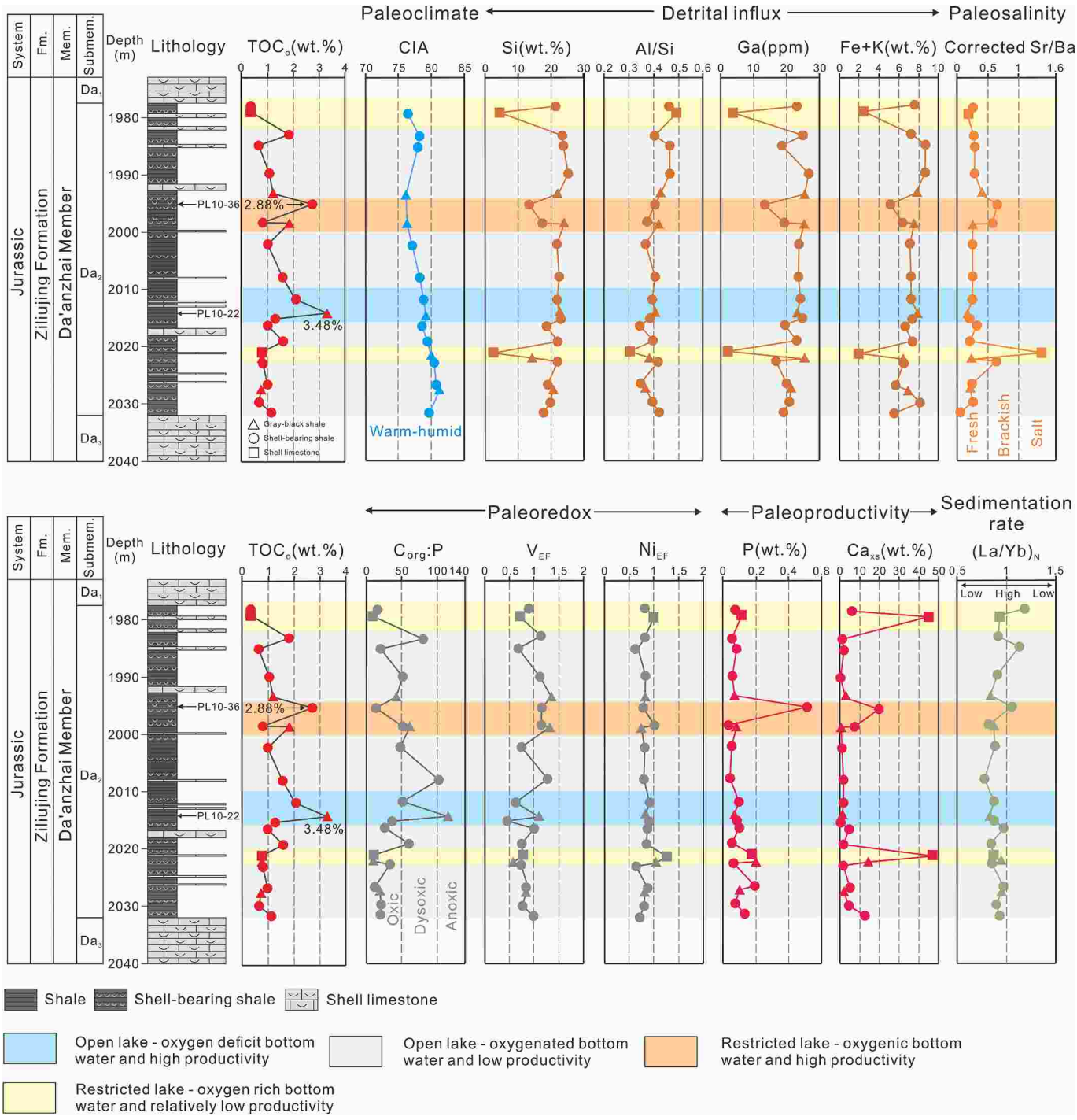

Fig. 6. Variations in the geochemical proxies of the Da'anzhai Member for well PL10. The semitransparent boxes indicate the four sedimentary periods of the paleolake. Light gray boxes indicate the open lake period bearing oxic bottom water with low productivity. Light blue ones indicate the open lake period with oxygen deficit bottom water conditions and high productivity. Light yellow ones indicate the restricted period with oxygen-rich bottom water conditions, and orange ones indicate the period of a restricted paleolake with high oxygen bottom water and high productivity. Fm. = Formation, Mem. = Member, and Submem. = Submember. (For interpretation of the references to colour in this figure legend, the reader is referred to the Web version of this article.)

Wei et al. (2018) was adopted in this study. However, the detailed process is not mentioned in the paper. Here, the calibration process in detail is described based on Wei et al. (2018). (1) Firstly, the relationship model between Sr and Ca content was established to judge the influence of carbonate minerals on Sr content in sediments. If Sr and Ca show a positive correlation ($R^2 > 0.64$), it is believed that the increase in carbonate minerals will cause excessive enrichment of Sr in sediments. (2) According to the relationship between Sr and Ca of samples, the baseline value of Sr content and the regression equation $Sr_{sample} = f(Ca_{sample})$ between Sr and Ca in sediments can be determined (Fig. 9). The baseline values indicate the amount of Sr absorbed in fine-grained sediments under the influence of low carbonate minerals. (3) Because the total amount of Sr in sediments is the sum of the content of Sr in fine-grained sediments and that of Sr in carbonate minerals, a formula for calculating the Sr abundance captured by carbonate minerals can be established (Eq. (5)). (4) The calculation model of corrected Sr content was defined

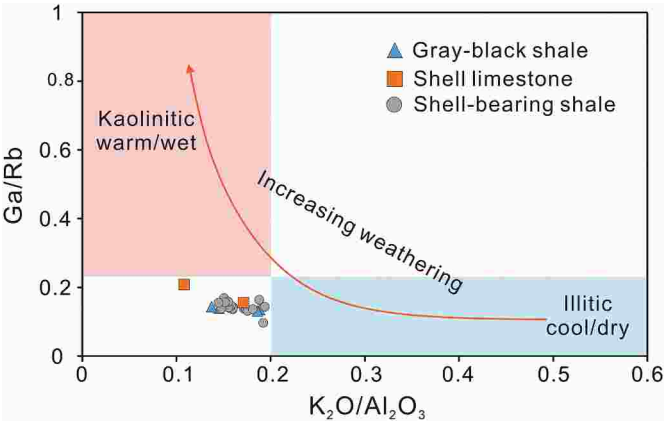

Fig. 7. Ga/Rb–K_2O/Al_2O_3 diagram for the Da'anzhai shale indicating a warm and humid climatic condition.

by removing the Sr content captured by carbonate minerals from the total Sr in the samples (Eq. (6)).Where $Sr_{carbonate}$ is Sr content captured by carbonate minerals, ppm; Ca_{sample} is the overall Ca content of the sample, %; $f(Ca_{sample})$ is the regression equation of Sr_{sample} and Ca_{sample}; $Sr_{Baseline}$ is the Sr element baseline value, ppm; $Sr_{corrected}$ is the Sr content of the sample after correction, ppm; Sr_{sample} is the overall Sr content of the sample, ppm.

The original Sr/Ba ratios are clustered between 0.25 and 4.38 with an average of 0.81, which indicate wide paleosalinity variations that range from fresh to salt aqueous conditions (Table 4). The initial data samples in the crossplot of Sr versus Ba are scattered into freshwater, brackish, and saltwater areas (Fig. 10). In contrast, the corrected Sr/Ba ratios range from 0.02 to 1.35 with a mean of 0.33, indicating that the salinity was consistent with freshwater with occasional brackish water (Table 4, Fig. 6). Moreover, the corrected shale samples are concentrated in the freshwater field, which is consistent with the Xujiahe shale (Fig. 10). The distinct difference between the bulk Sr/Ba ratios using the corrected Sr contents and initial bulk Sr/Ba ratios in the Da'anzhai shale suggests the influence of the biogenic carbonate Sr fractions on the bulk Sr/Ba ratios (Fig. 10).

The vertical distribution of the initial Sr/Ba ratios shows a completely opposite trend to the CIA values, and its abrupt transition to intense saltwater conditions correspond to climatic and lithological changes (Fig. 6). However, the Da'anzhai Member was an open lake system that reached a maximum flooding period and the shale was deposited in a typical cratonic basin of the Sichuan Basin (Hieronymus et al., 2001). It is considered that such a paleosalinity transition did not

Table 4
Paleoenvironmental proxies for the Da'anzhai lacustrine shale from well PL10.

Sample No.	Depth (m)	TOC_o (%)	CIA	Al/Si (%)	Si (%)	Ga Ppm	Fe + K (%)	Sr/Ba*	Sr/Ba	C_{org}:P	V_{EF}	Ni_{EF}	P (%)	Ca_{xs} (%)	$(La/Yb)_N$
PL10-6	2031.58	0.99	/	8.30	19.46	19.12	5.54	0.02	0.44	23.41	0.98	0.72	0.13	12.80	0.93
PL10-7	2029.8	0.60	80.41	9.29	23.54	20.86	8.12	0.23	0.50	25.03	0.78	0.81	0.07	4.41	0.89
PL10-9	2027.5	0.69	81.29	9.70	26.64	21.44	6.97	0.20	0.42	22.25	0.84	0.83	0.10	1.91	0.95
PL10-10	2026.7	0.86	80.74	8.88	25.04	20.16	5.63	0.23	0.56	13.86	0.84	0.88	0.19	4.95	0.97
PL10-12	2022.7	0.73	/	10.30	24.55	16.78	6.51	0.61	0.76	39.83	0.73	0.64	0.06	1.53	0.85
PL10-13	2022.2	0.71	80.05	8.27	21.54	24.62	6.36	0.28	0.28	10.95	0.59	1.16	0.20	13.30	0.94
PL10-14	2021.1	0.69	/	1.07	3.51	1.80	2.13	1.36	4.35	11.94	0.79	1.50	0.18	47.38	0.87
PL10-17	2019.1	1.41	/	10.32	26.09	23.40	7.33	0.18	0.30	71.44	0.75	0.87	0.06	1.84	0.85
PL10-19	2016.4	0.89	78.56	8.74	25.46	19.40	6.53	0.32	0.60	30.06	1.00	0.88	0.09	4.68	0.97
PL10-20	2015.2	1.14	79.24	10.77	27.66	24.98	7.32	0.19	0.27	42.56	0.45	0.90	0.08	0.21	0.88
PL10-22	2014.27	2.90	79.24	10.61	26.16	23.52	7.84	0.16	0.25	137.13	1.09	0.85	0.07	0.96	0.84
PL10-24	2011.8	1.82	78.86	10.31	26.21	24.22	7.21	0.23	0.35	61.47	0.61	0.92	0.09	1.75	0.86
PL10-27	2007.8	1.38	/	10.55	25.83	23.70	7.22	0.24	0.35	122.36	1.26	0.81	0.03	1.99	0.78
PL10-30	2002.2	0.90	77.08	10.19	27.70	23.72	7.11	0.23	0.35	58.03	0.75	0.83	0.05	1.03	0.88
PL10-32	1998.6	1.61	76.29	11.23	26.59	25.62	7.55	0.23	0.28	71.37	1.30	0.74	0.07	0.34	0.87
PL10-33	1998.5	0.72	75.59	8.18	21.68	19.39	6.40	0.59	0.88	63.84	1.14	1.00	0.03	7.48	0.83
PL10-36	1995.3	2.40	/	6.24	15.36	13.22	5.19	0.64	1.41	14.55	1.17	0.80	0.51	20.06	1.05
PL10-37	1993.4	1.07	76.10	10.52	24.73	25.54	7.68	0.41	0.51	50.60	1.36	0.83	0.07	2.91	0.84
PL10-40	1989.8	0.94	79.27	11.83	25.48	26.94	8.58	0.26	0.29	60.61	1.11	0.84	0.05	0.52	0.91
PL10-43	1985	0.58	77.93	11.19	24.19	18.65	8.69	0.27	0.37	24.20	0.68	0.63	0.07	1.96	1.14
PL10-45	1983.1	1.60	78.16	10.96	27.13	25.36	7.19	0.26	0.32	94.58	1.15	0.82	0.05	0.41	0.92
PL10-48	1979.2	0.35	/	1.97	4.01	3.55	2.46	0.15	4.38	9.55	0.72	1.03	0.11	44.64	0.93
PL10-50	1978.1	0.32	78.93	10.13	21.77	23.12	7.54	0.24	0.47	15.13	0.89	0.82	0.07	6.11	1.18

Note: "/" means no detected data. Sr/Ba* is the ratio using corrected Sr for the calculations.

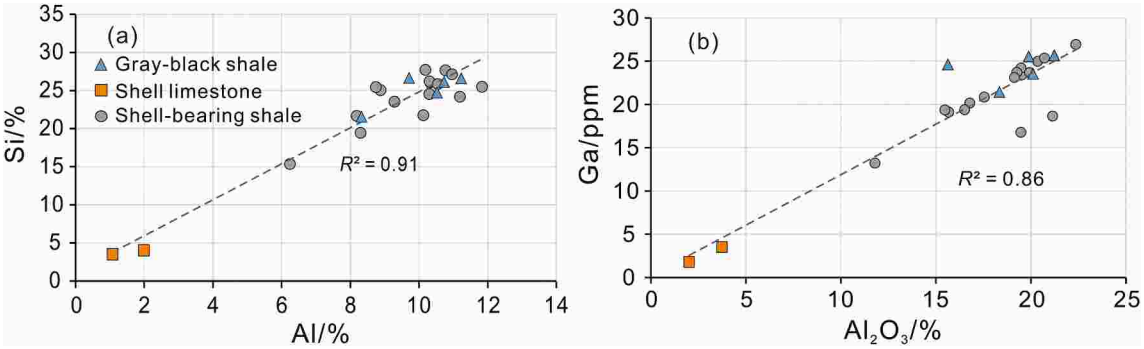

Fig. 8. Correlations between different indicators. (a) Si (wt.%) versus Al (wt.%), and (b) Ga (ppm) versus Al_2O_3 (wt.%).

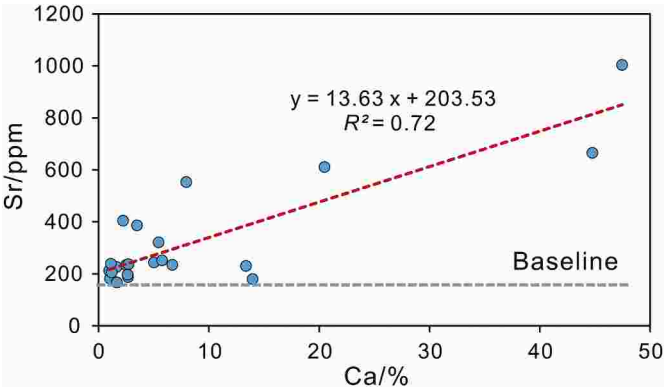

Fig. 9. Linear regression equation between Sr and Ca content, and the baseline value of Sr content.

$$Sr_{carbonate} = f(Ca_{sample}) - Sr_{Baseline} \quad (5)$$

$$Sr_{corrected} = \begin{cases} Sr_{sample} - Sr_{carbonate}, Sr_{carbonate} \le Sr_{sample} \\ Sr_{sample} \quad , Sr_{carbonate} > Sr_{sample} \end{cases} \quad (6)$$

occur readily in the overall stable, warm and humid climate during the Da'anzhai period, except that crustal movement events or extreme climatic variations resulted in a surge and vast increase in evaporation and decrease in precipitation, which led to the regression of the lake and a dramatic rise in salinity. Furthermore, freshwater lacustrine bivalve fossils are plentiful in sediments, most of which belong to *Pseudocardinia* (Cai, 1998). Therefore, it is inferred that the lithological variations resulted from sedimentary facies changes that were caused by the migration of lakeshores, which caused the lake water depths to decrease slightly and the distances required for rivers to enter the lake to increase. As a result, the lithology that is related to biological shells was deposited in a shallow lake with a lack of terrigenous detrital components, which provided an important contribution to Sr uptake by precipitated carbonate. The depositional environment of the Da'anzhai shale was dominated by warm and humid climates in an open lacustrine system and should be stable and consist mainly of freshwater. This investigation of the paleowater conditions via the elemental concentrations for the Da'anzhai shale reveals the feasibility and reliability of the corrected bulk Sr/Ba ratios as a paleosalinity indicator.

5.2.3.2. Paleoredox. Distinguishing the redox facies for shale formations is based on analyzing the sensitivities of sediment chemistries, biogeochemical cycles and organic carbon accumulations (Bennett and Canfield, 2020; Algeo and Li, 2020). The bimetal ratios of V/Cr, U/Th, Ni/Co, and Ni/V can be used for paleoredox analyses (Jones and Manning, 1994; Rimmer et al., 2004). The principle behind their applications is that one element is more authigenically enriched under anoxic conditions than the other element. The good performance of trace-metal element EFs as redox proxies (such as Co_{EF}, Cr_{EF}, Cu_{EF}, Ni_{EF}, Pb_{EF}, U_{EF}, and V_{EF}) has been successively confirmed (Brumsack, 2006; Algeo and Liu, 2020). Because all transition-group metal elements are prone to authigenic enrichment under reducing conditions, Algeo and Liu (2020) reported a potential issue that bimetal ratios as redox proxies may not achieve the efficiency of the ratios of metals to redox-insensitive elements. Nevertheless, the thresholds of the trace metal elemental ratios proposed by Jones and Manning (1994) are still widely used in recent studies (Smolarek et al., 2017; Lu et al., 2019). What needs attention and avoidance is that there is no universal proxy that can determine redox conditions by fixed thresholds owing to variable deposition factors in different sedimentary systems, such as the differences in mineral compositions and types of OM, sedimentation rates, water mass conditions and other factors (Algeo and Rowe, 2021). Therefore, interpretations of the redox conditions of bottom waters should be conducted based on the local target investigated formations and rely on multiple redox proxies to reduce uncertainties (Algeo and Liu, 2020).

Hydrothermal fluids are likely to alter some metal element concentrations in redox cycles (Morford et al., 2005). The elemental contents related to terrigenous debris merely reflect the chemical characteristics of the provenance region. Hence, it is more reliable to use authigenic elements to restore paleosedimentary environments (Tribovillard et al., 2006). Accordingly, identifying the origin and source of the elements is a significant step. A practical way to distinguish elemental origins is based on the correlations of aluminum and other elements (Calvert and Pedersen, 1993; Tribovillard et al., 2006), which suggests that: (1) a strong positive correlations ($R > 0.6$) indicate that the elements originating from a provenance are dominant, (2) elements are authigenic, biogenetic, or hydrogenous sources owing to the prominent negative correlations with Al ($R < -0.6$), and (3) low correlations (e.g., absolute values of $R < 0.6$) may result from the combined action of multiple elemental sources. It is worth noting that this calculation excludes two shell limestone samples with low Al contents, PL10-14 and PL10-48 (Al, wt.% = 1.07 and 1.97, respectively), which may cause a significant increase or decrease in the correlation. According to the results of the correlation coefficients for the elements used in the present study (Appendix Table A1), the trace elements, including Cr, Co, Ni, Ga, and Rb, are divided into detrital groups; Ca and P metal elements are regarded as authigenic and biogenetic groups; and the residual elements Ba, V, Cu, Zr, Nb, Hf, Ta, Pb, Th and U are mixed sources.

In this study, the efficient proxies and EFs of the trace metal elements, such as Co_{EF}, Cr_{EF}, Cu_{EF}, Ni_{EF}, Pb_{EF}, U_{EF}, and V_{EF}, are unfortunately limited for the following reasons: (1) mixed origins are likely to potentially increase the uncertainty of the interpretation, (2) the detrital

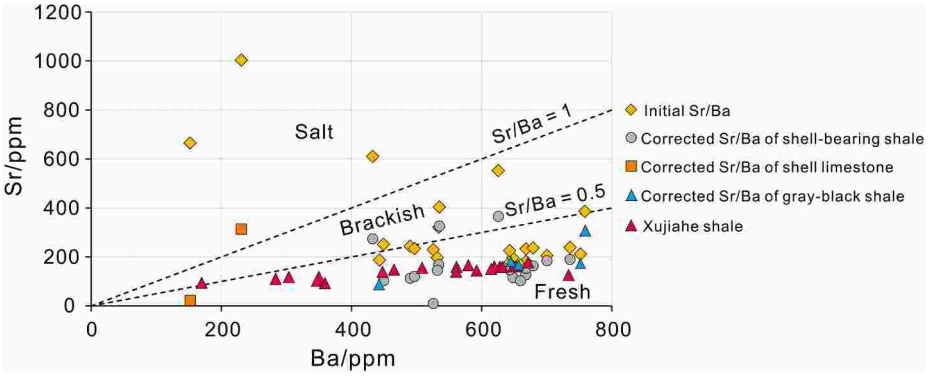

Fig. 10. Crossplot of Sr versus Ba illustrating paleosalinity by comparing corrected Sr/Ba with initial bulk Sr/Ba. The Xujiahe continental shale was deposited in a freshwater environment with Sr/Ba ratios averaging 0.29 (Yang et al., 2019).

elements record most of the chemical information from the provenance, and (3) the EFs are approximately equal to 1, which suggests that the degree of enrichment of these elements is comparable to the background and reflects the limited effect of redox conditions. Naturally, reduced reliability would occur when using the bimetal ratios derived from these elements as redox proxies (e.g., V/Cr, U/Th, Ni/Co, Ni/V). Therefore, we adopted the proxy C_{org}:P (calculated on a molar basis) to infer the redox conditions based on the C–S–Fe–P system. Phosphorus prefers to be released under anoxic conditions from OM rather than carbon due to the reductive dissolution of ferric hydroxide, and P is preserved in sediment uptake by Fe-oxyhydroxides under oxic conditions (Murphy et al., 2000; Algeo and Ingall, 2007). Elevated C_{org}:P ratios indicate an improvement in the degree of reducing conditions, and their values of <50, 50–100, and >100 correspond to oxic, dysoxic and anoxic conditions, respectively (Algeo and Ingall, 2007).

A lack of enrichment or slight enrichment of V and Ni relative to the PAAS is considered as a signal of oxic conditions, although these proxies cannot reliably indicate redox environments (Bennett and Canfield, 2020) (Fig. 6). Thus, the Cr_{EF}, Cu_{EF}, Ni_{EF}, Pb_{EF}, U_{EF} and V_{EF} values of the Da'anzhai shale provide sparse information to imply oxygenated conditions owing to EFs that are close to 1 (Fig. 5). Because of the polygenetic origin, these EFs may not reflect the details of redox conditions, but they can enlighten the explanation of paleoredox status. Rather, the C_{org}:P values in the Da'anzhai shale record relatively detailed fluctuations, which thereby reflect oscillating redox conditions to organic accumulation.

The profile of the C_{org}:P ratios for the Da'anzhai calcareous shales shows frequent fluctuations with a range from 9.55 to 137.13 and an average of 46.73, indicative of the dominance of oxic conditions (Fig. 6). P is occasionally abundant, yielding maximum P_{EF} values up to 23.82 with a median of 0.95. Furthermore, the P_{EF} and Ca_{xs} profiles have notable similarities with a positive correlation (R^2 = 0.76, Fig. 11, Fig. 6), which implies high oxygen contents in the water mass, as evidenced by the high biomass and abundant trace fossils (e.g., *Palaeophycus*) in the paleolake (Zhang et al., 2018). Large quantities of dissolved oxygen penetrate into bottom sediments due to the overturning of water-column-breaking stratification (Xu et al., 2013). Such interactions among biological and hydrodynamic factors enhance sedimentary P accumulations and retention at the water-sediment interface under oxidizing conditions (Ingall et al., 2005). The lack of P and low C_{org}:P in sediments illustrates the high dissolved oxygen contents and low sinking fluxes of organic matter in the paleolake, which may be due to the limited nutrient sources in this period. In contrast, low enrichments or loss of P (the minimum of P_{EF} = 0.47) with high C_{org}:P ratios that are greater than 100 and low levels of Ca_{xs} contents at the ~2000 m–2015 m stratigraphic levels (Fig. 6) suggest abundant released sedimentary P from OM under oxygen-deficient conditions (Algeo and Ingall, 2007) and enhanced reduction via continuous OM decomposition (Tribovillard et al., 2006).

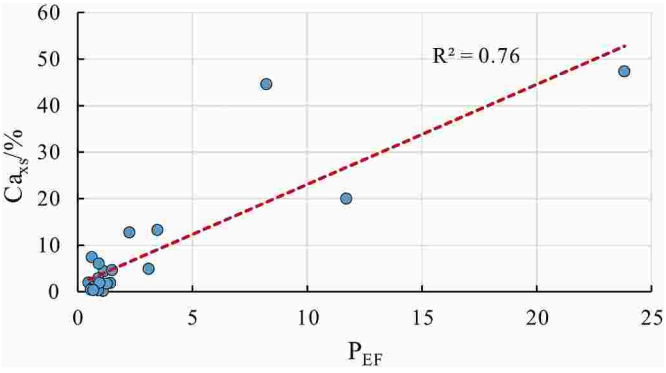

Fig. 11. P_{EF} versus Ca_{xs} (wt.%) concentrations for the Da'anzhai lacustrine shale, which are indicative of the relationship between the lake water oxygen contents, biological abundances and P preservation.

With respect to the minerals, framboidal pyrite that forms near the redox interface is of great significance in retrieving paleoredox environments (Wignall and Twitchett, 1996). Bond and Wignall (2010) summarized the framboid characteristics used to determine redox conditions during deposition. Framboids dominate the pyrite fraction with small particle sizes averaging 3–5 μm and form above the water/sediment interface under euxinic conditions (Liu et al., 2019). Anoxic settings are characterized by abundant small framboid pyrites with mean sizes of 4–6 μm. A few large framboids and some crystalline pyrite mainly develop in the sediments below the water/sediment interface under dysoxic environments (Wilkin and Barnes, 1997), with mean sizes of 6–10 μm. No framboid pyrites occur under oxic conditions. For sample PL10-22, the sizes of the framboid pyrite clusters between ~7 and 10 μm at a depth of 2014.3 m corresponding to a high C_{org}:P value range, which further supports the presence of dysoxic-anoxic bottom water (Figs. 6 and 12a). Some euhedral pyrites can be observed in Fig. 12a and they crystallized due to the enhanced reducing degree of the pore waters at the early diagenetic stage. In contrast, euhedral pyrites commonly formed in sediments under pore water reduction during the early diagenetic stage, indicative of the redox interface was below the sediment/water interface and oxic bottom water conditions. As shown in sample PL10-36, the majority of the pyrites are euhedral pyrite with a low C_{org}:P value and high TOC_o (Fig. 12b, Table 4), which indicates that the bottom water had a high oxygen content and that the sediments at the water/sediment interface experienced oxidization to some extent. Then, the sediments below the sediment/water interface underwent reduction via the oxidation of organic carbon consuming oxygen in the pore water (Morford et al., 2009). Therefore, it is possible that high TOC levels can be retained in sediments within oxic aquatic environments under the conditions of sufficient OM inputs and rapid sedimentation rates (Ganeshram et al., 1999; Tyson, 2001).

To sum up, the Da'anzhai calcareous shale was deposited in a variable redox environment, in which the bottom water usually exhibited oxidizing conditions due to the photosynthesis of algae in the euphotic zone or due to high oxygen contents in the atmosphere with a lack of stratification. A dysoxic or weakly oxygenated bottom water occurred owing to the stable and relatively deep paleolake providing temporary lentic bottom water conditions (Fig. 6).

5.2.4. Paleoproductivity

The accumulation of OM in sediments strongly relies on the primary productivity based on biological contributions in the surface water of lake systems (Murphy et al., 2000). The trace elements P and Ba are the main nutrient elements for aquatic organisms and are commonly used to evaluate the primary productivity of paleolakes (Morel and Price, 2003; Brumsack, 2006).

Phosphorus is an important component of living creatures (Haddad and Martens, 1987) and is normally derived from plankton and biological skeletons in sediments. The P levels in the Da'anzhai shale exhibit a remarkable negative correlation with the Al contents, which is indicative of its biogenetic origin. The P concentrations received some appreciable amounts of augmentation throughout the whole shale succession, which range between 0.03% and 0.51% (Fig. 6, Table 2). In Section 5.2.3.2, the occurrence of P enrichment in sediments that were deposited in bottom water with high dissolved oxygen contents is discussed, which was accompanied by a surge in biogenetic calcium (Ca_{xs}) due to shellfish remains (Fig. 6). Thus, this phenomenon supports the view that there was a bloom of massive algae and benthic shells in the euphotic zone in the Da'anzhai paleolake, which brings about relatively high primary productivity (Fig. 13b) (Xu et al., 2020). Moreover, the lack of P with high TOC_o in the sediments indicates enhanced P recycling, that is, P rediffused into the water column under reducing conditions (Ingall et al., 2005) and improved the resupply of nutrients to increase the primary productivity. The strong P recycling ensures the preservation of organic carbon (Xu et al., 2020; Shen et al., 2015)

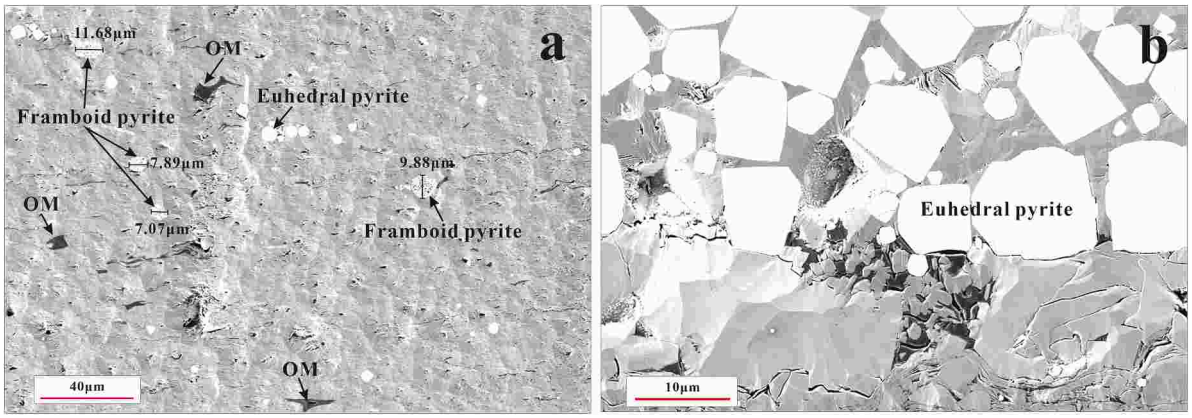

Fig. 12. Analysis of the characteristics and pyrite types; (a) a few and moderate framboid pyrites with a size range of ~7–10 μm, some euhedral pyrites and OM are observed in sample PL10-22, 2014.3 m and (b) the majority of pyrite consists of euhedral crystals formed in sediment under pore water reduction during the early diagenetic stage, indicative of the redox interface was below the sediment/water interface. PL10-36, 1995.3 m.

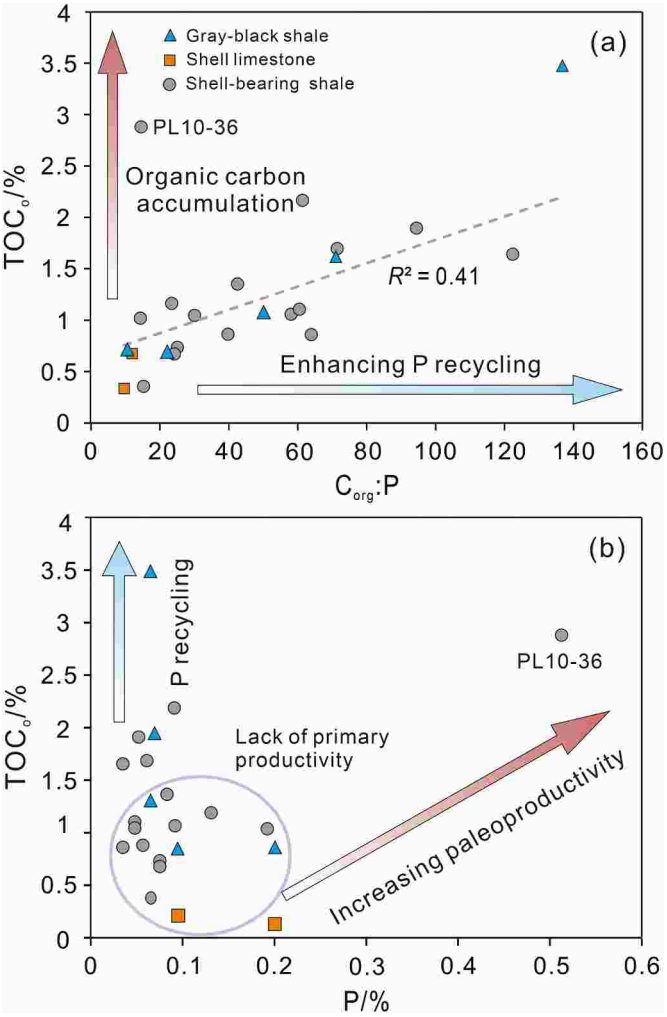

Fig. 13. Crossplots of (a) TOC_o versus C_{org}:P values and (b) TOC_o versus P concentrations. Different chemical behaviors of P as a paleoproductivity proxy under different conditions.

(Fig. 13a and b). However, the P content is kept at low levels in oxic bottom waters with commonly low TOC_o values, which implies that the relatively weak nutrient supplies and low sinking influxes of particulate organic carbon in open paleolakes resulted in low primary and export productivity (Fig. 13b).

In addition to P, Ba has been widely used as a paleoproductivity indicator (e.g., Dymond et al., 1992). The Ba in dissolved or particulate form within aquatic systems originates from weathering of sedimentary and igneous rocks. Barite, which plays a critical role in biogenic Ba collection, is formed due to decaying phytoplankton (i.e., diatoms) in the water column (Bishop, 1998), which supports the view that planktonic organisms play a role in the Ba cycle (Sternberg et al., 2005). Therefore, the concentrations of biogenetic Ba correlate well with the productivity in paleolakes. Furthermore, barite can precipitate within enhanced concentrations of SO_4^{2+} that are caused by the oxidation of OM or H_2S (Schoepfer et al., 2015). Ba in the present study exhibits a moderate correlation with Al (R = ~0.6, Appendix Table A1). The origin of Si for the Da'anzhai shale is mainly from a terrigenous provenance subjected to weathering, which indicates a possibility weak uptake of Ba by diatoms. Thus, the high uncertainty in the Ba source may induce a variety of analytical results. Hence, Ba element will not be utilized as a paleoproductivity proxy for the Da'anzhai shale.

The mass propagation of benthic freshwater shellfish indirectly reflects the proliferation of algae, plankton and phytoplankton as nutrient sources. Considering the prominent feature of the development of shellfish and ostracoda fossils in the Da'anzhai calcareous shale and the strong positive relationship between P_{EF} and Ca_{xs} in the paleolake (Fig. 11), the hypothesis to regard biogenic Ca (Ca_{xs}) as a potential paleoproductivity indicator is strengthened (Murphy et al., 2000). However, in open paleolake, increased water depth could induce dysoxic bottom water conditions, which is not conducive to the enrichment of P in sediments and generally enhances active P recycling related to the increase in primary productivity and an adequate source of OM. Furthermore, shallow water rich in oxygen and nutrients favors the survival of shellfish. A lack of shell remains generally occurred under deep and quiet depositional conditions in the open lake. Therefore, biogenic Ca (Ca_{xs}) as a paleoproductivity proxy could be employed effectively in relatively shallow deposition mixed with calcareous organisms.

Thus, on the whole, high primary productivity requires high biomass of aquatic organisms in the euphotic zone (Ganeshram et al., 2003). The elevated paleoproductivity of shale in the Da'anzhai Member is intermittent (Fig. 6). Moreover, regardless of whether the bottom water is under oxidizing or reducing conditions, high export production depended on the rapid burial efficiency and preservation of OM during the deposition of the Da'anzhai shale, but the standards in oxic environments were relatively higher.

5.3. Controls on organic accumulation in lacustrine shale in paleolakes

OM accumulations are effectively controlled by multiple factors in the depositional environment, including paleoclimate, paleoproductivity, detrital input, paleoredox and sedimentation rate (Sageman et al., 2003; Liang et al., 2020).

As discussed in the previous section, the Da'anzhai Member was a typical freshwater open lake during deposition (Wang et al., 2006). In addition, the shale deposition period was dominated by a warm and humid paleoclimate with a low level of fluctuation (Fig. 6). Warm and humid climate is favorable to the growth of aquatic organisms and boosts primary productivity, which in turn promotes the enrichment of OM (Prokopenko et al., 2001). However, a lack of correlation occurs between the paleoclimate and TOC_o in the Da'anzhai shale (Fig. 14a), which indicates that the accumulation of OM was the result of the integrated effects of hydrodynamic, biological and other factors. Similarly, freshwater conditions have no potential impact on OM, as evidenced by the paleosalinity being unrelated to TOC_o (Fig. 14b).

Sedimentation rates serve as another important factor that can have a potential influence on OM accumulations (Ibach, 1982). A high sedimentation rate stage will induce a dilution effect, which thereby hinders the enrichment of OM (Tyson, 2001). Previous studies have reported that the average sedimentation rate of the Da'anzhai shale was ~150 m/Ma (Li, 2016). The $(La/Yb)_N$ values can be used to indicate sedimentation rates (Goodarzi and Gentzis, 2018; Lei et al., 2021). If the $(La/Yb)_N$ ratio is concentrated around 1, the sedimentation rate is high. On the contrary, the ratio is far away from 1, indicating a low sedimentation rate (Liu et al., 2022). As shown in Fig. 14c, all data points nearly locate in the areas that represent relatively high sedimentation rates, with the TOC_o values distributed discretely under the same sedimentary background, which indicates that the sedimentation rate was not a direct controlling factor for OM enrichment. Nonetheless, high sedimentation rates provide the key geological conditions for the burial and preservation of OM in oxygen-rich bottom water, achieved by reducing oxygen exposure, even if dilution occurs (Ganeshram et al., 1999; Tyson, 2001; Mansour et al., 2020). Such circumstances existed during the Da'anzhai shale deposition process. For example, sample PL10-36 is characterized by high TOC_o and oxidized bottom water at the same time (Figs. 6 and 13a). Moreover, the terrestrial debris inputs for the Da'anzhai shale are relatively high, except for two shell limestone samples and sample PL10-36 (Fig. 14d). In a warm climate with high rainfall, sediment debris such as plant debris and OM particles will be injected into lakes through rivers, which thereby improves the OM conditions in lakes (Murphy et al., 2000). Therefore, it can be observed from Fig. 14d that high TOC_o tends to develop under high detrital conditions. However, notably, a decrease in the input of detrital influx is recorded at a depth of 1995.3 m with high TOC_o contents (sample PL10-36), which suggests that organic carbon accumulations can be independent of high terrigenous OM inputs. This sample has the feature shown by the high black mud contents with a lack of sandy clastics, abundant shellfish debris due to storm flows, and large numbers of recrystallized columnar calcites that formed in the residual spaces owing to the dissolution of shells during diagenesis (Fig. 3f). Thus, organic-rich shale, such as that in sample PL10-36, can develop with relatively low terrestrial inputs, possibly due to relatively weak dilution, high paleoproductivity and burial efficiency (Fig. 13a and b, Fig. 14d).

Elevated primary paleoproductivity is a necessary condition for the formation of organic-rich shale, but it does not play a decisive role in the formation of organic-rich shale (Fig. 13b). As discussed in Sections 5.2.3 and 5.2.4, OM enrichment could occur when the bottom water was oxygen-rich or oxygen-deficient (Fig. 13a and b), which suggests that the role of paleoredox as a condition for preservation or destruction

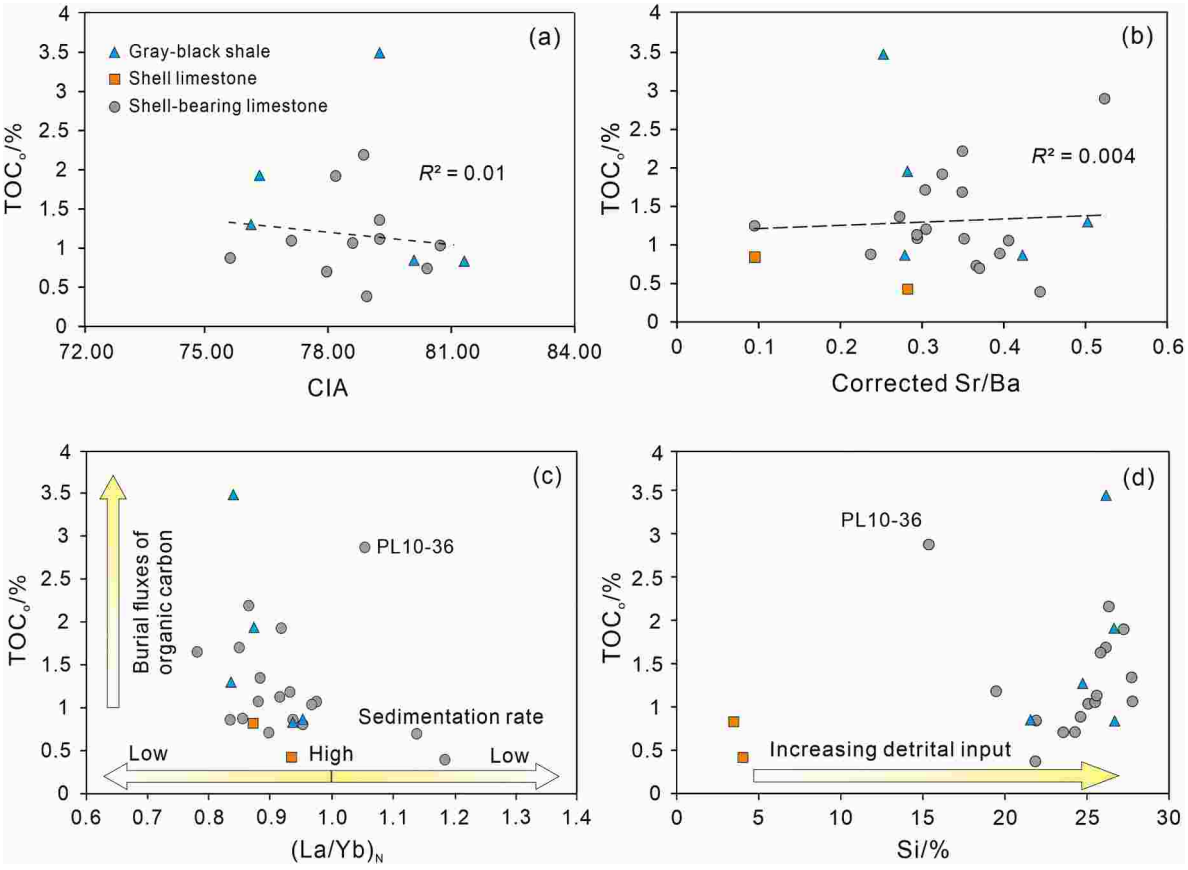

Fig. 14. Crossplots of different proxies and TOC_o suggesting the controlling factors on organic matter accumulaition. (a) TOC_o (wt.%) versus CIA, (b) TOC_o (wt.%) versus corrected Sr/Ba, (c) TOC_o (wt.%) versus $(La/Yb)_N$, and (d) TOC_o (wt.%) versus Al (wt.%).

needs to consider the relationship between the degree of exposure in the water environment of OM and its quantity.

In summary, the differences in paleoproductivity and paleoredox under the climatic conditions and deposition rates fundamentally determine the export production and preservation efficiency of organic carbon and ultimately controlled OM enrichment during the deposition of the Da'anzhai calcareous shale.

5.4. Models of organic accumulation for lacustrine shale mixed with shell bioclasts

In consideration of the above discussion, the ancient lake mainly remained an open type. Three periods of restriction were induced by transitory lower levels of precipitation and stream recharge during Da'anzhai deposition (Fig. 6). The low C_{org}:P values in the sediments indicate high oxygen contents in the open paleolake water mass, which resulted in the enhanced degradation of OM (Fig. 13a and b). Moreover, due to the combined effects of reduced paleoproductivity and strong OM decomposition, OM particles could not effectively accumulate and be preserved in the sediments in the open paleolake with oxygenated bottom water (Fig. 6). Similarly, owing to the shallowing of the lake water, weak stratification, reduced terrigenous detrital input in the paleolake during the restriction period, the bottom water remained highly oxygenated and provided no conditions for OM preservation and accumulation (Fig. 6). Therefore, the enrichment of OM was difficult to achieve due to the negative effects of decomposition and dilution for the Da'anzhai lacustrine calcareous shale. However, the increased TOC_o values observed on the geochemical profile correspond to two sedimentary backgrounds (Fig. 6): one was an open paleolake with reduced bottom water conditions and high paleoproductivity, and the other was a restricted paleolake with oxidizing bottom water conditions and high productivity, thereby revealing the existence of different OM enrichment mechanisms.

(1) Open paleolake with dysoxic bottom water conditions and high productivity

A warm and humid climate has the advantage of OM accumulation. Abundant river water carries terrestrial debris but also continentally derived OM and nutrients (e.g., P and N). The lack of a correlation between the TOC_os and detrital proxies in the Da'anzhai lacustrine shale indicates that the input of the siliciclastic fractions had a limited influence on the TOC contents through dilution. Conversely, an elevated influx can certainly promote the enrichment of OM (Fig. 14d). Active P recycling induced by oxygen deficit bottom water conditions proves the increase in primary productivity and an adequate source of OM (Fig. 15a). Furthermore, aerobic OM decay principally controls the concentrations of sinking organic carbon particles (Simon et al., 1994). Depending on the good preservation condition, the sedimentation rate too fast or too slow is not conducive to the enrichment of organic matter (Müller and Suess, 1979; Ingall and Van Cappellen, 1990; Liu et al., 2022). The $(La/Yb)_N$ shows a range of 0.78–0.84 during this period, which indicates moderate sedimentation rate and avoids substantial dilution of organic matter (Fig. 6). Thus, the open paleolake system exhibits oxygen-deficient bottom water with high paleoproductivity and moderate sedimentation rate, which suggests that lower OM degradation levels, enhanced P recycling and weak dilution ensure organic carbon accumulation and preservation during deposition (Figs. 6, 13a and 15a).

(2) Restricted paleolake with oxidizing bottom water conditions and high productivity

The climatic conditions gradually became cold and arid, which directly resulted in reduced precipitation and indirectly induced decreased weathering levels and decreases in stream flow. Meanwhile, the fluxes of terrigenous siliciclastics and nutrients diminished (Dittmar and Kattner, 2003; Liu et al., 2020) (Fig. 6). The weak river input fluxes and other water supplies caused the paleolake to shift from open to restricted (Fig. 15b). However, the enhanced primary productivity seems to have been unaffected by external supplies (Fig. 6). In surface freshwater systems, phosphate is considered to be the limiting factor for algae and plankton growth (Xu et al., 2010). The decay of algae and plankton residues releases large quantities of nutrients into the water environment for a new generation of algae, which may cause supersaturation of dissolved oxygen in lakes and thereby endanger other aquatic organisms (Lin et al., 2020). A remarkable positive correlation between Ca_{xs} and P_{EF} was observed in the Da'anzhai sedimentary period (Fig. 11), which indicates that the death of shells due to a eutrophication event, and the high oxygen content allowed P to be preserved in the sediments (Fig. 15b). Therefore, the transitory restriction of the paleolake brought about high primary and export productivity and ensured that sufficient amounts of OM particles were deposited on the lake bottom and were weakly subjected to dilution (Fig. 15b). Moreover, the high sedimentation rate accelerated the burial of OM and shortened the time for OM to be oxidized. During early diagenesis, the oxidation of OM will exhaust the oxygen in pore waters, which transforms the redox state toward reduction below the water/sediment interface and results in the formation of abundant euhedral pyrites (Simon et al., 1994) (Figs. 15b and 12b). As such, under the conditions of a restrictive paleolake, a sink of plentiful OM particles, rapid sedimentation rate and decomposition of OM ought to be required to maintain the enrichment conditions for residual OM in the Da'anzhai Member.

6. Conclusion

The complete suite of lacustrine calcareous shale successions with shell bioclasts provided new insights into the synergistic influence of environmental conditions in different enrichment processes of organic matter and the geological significance of shell bioclastic contents in sediments.

The Da'anzhai paleolake was dominated by a warm and humid climate with high detrital influxes, as evidenced by intense chemical weathering and a long-term freshwater environment. The fine-grained sediments in the bottom water experienced varied redox conditions due to the changes in climate and hydrography under the background of rapid sedimentation rates. Furthermore, the primary and export production was highly dependent on a water mass bursting with aquatic life in the euphotic zone and the circulation of nutrients.

The importance of rapid deposition and burial to organic matter accumulations in oxygenated bottom water was confirmed by the application of paleoenvironmental proxies for the Da'anzhai shale in the central Sichuan Basin. The climate changed to cold and arid, which resulted in a transitory restriction for the paleolake. This caused a high biomass level consisting of lower aquatic organisms and offered high primary and export production and high organic carbon sinking influxes under high sedimentation rates. The enhanced the efficiency of organic matter accumulation eventually allowed abundant organic matter to be preserved in the oxic bottom water. In addition, in the open paleolake, the low oxygen content in the bottom water restrained organic matter degradation. Enhanced P recycling, moderate sedimentation rate and high detrital inputs ensured that large amounts of organic matter were imported and preserved in sediments. Therefore, in summary, the high primary production and sedimentation rates were the keys to the organic carbon enrichment in the Da'anzhai shale with shell bioclasts.

Ca in the Da'anzhai Member came from the freshwater shells in the lake. The remarkable enrichment of P and Ca proves the existence of a eutrophication event and the massive death of benthic calcareous organisms in the lake. Such an event supports the hypothesis that biogenic Ca (Ca_{xs}) can be regarded as a potential paleoproductivity indicator to some extent.

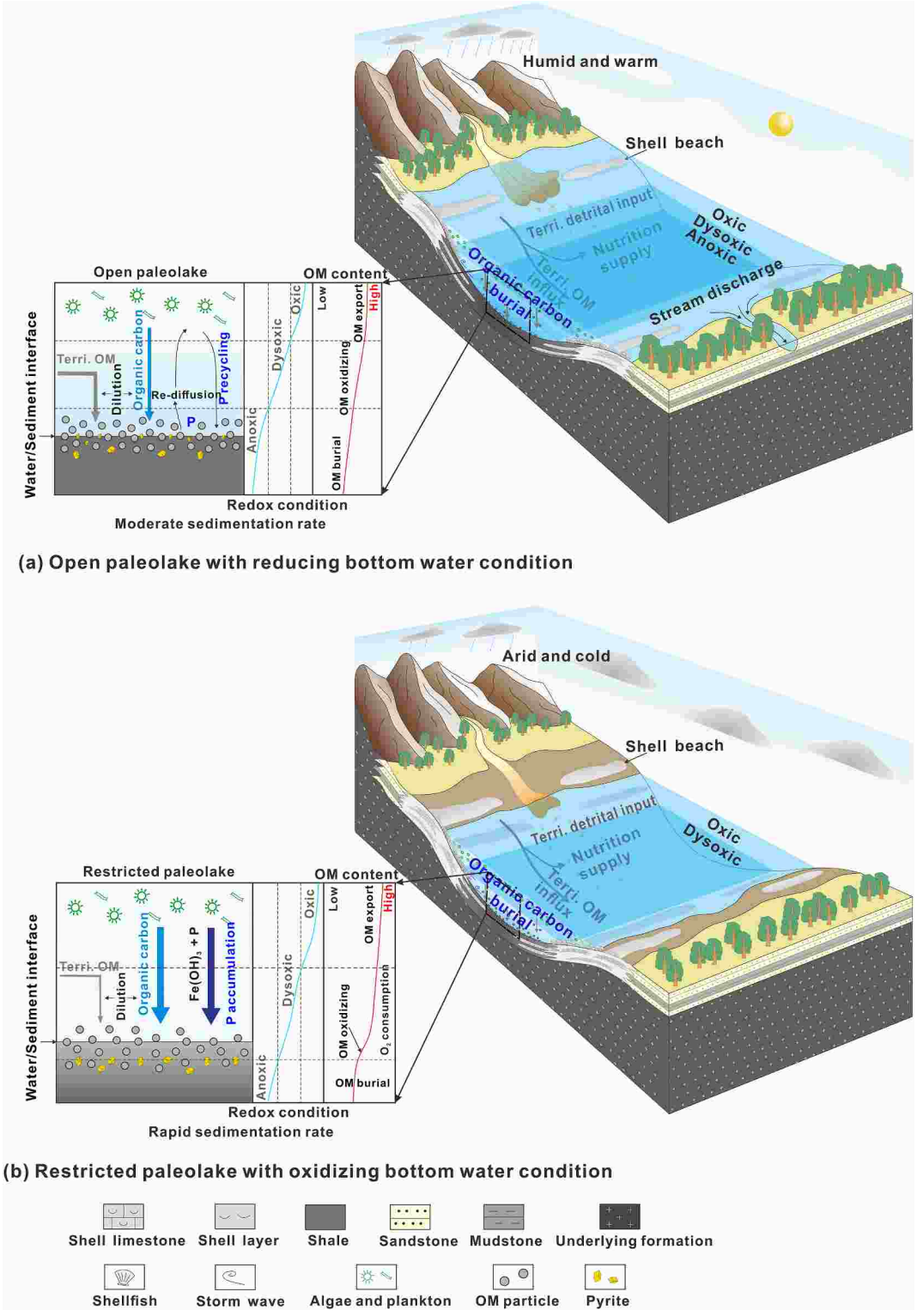

Fig. 15. The organic-rich shale formation and OM enrichment model for the Da'anzhai Member; (a) The warm and humid climate provided abundant rainfall that resulted in a deep and stratified paleolake, which allowed the ancient lake to receive large amounts of terrestrial input and algae to multiply in the surface water. This ensured that high amounts of OM particles were sinking. The anoxic bottom water provided good preservation conditions for OM and enhanced the recycling of nutrient element P in the water column. The moderate deposition rate, high OM influxes, high burial efficiencies and favorable preservation conditions promoted the enrichment of OM. (b) A climate that changed to cold and arid caused weak river input fluxes, which led to paleolake shifts to the restricted type. The high P and Ca concentrations in the sediments revealed a eutrophication event that offered high primary and export production, and the high organic carbon sinking influxes with high sedimentation rates strengthened the efficiency of OM accumulation in the oxic bottom water.

Author statement

Wenzhi Lei: Data curation, Writing – original draft, Methodology, Software. Dongxia Chen: Writing – review & editing, Supervision. Ziyi Liu: Resources, Formal analysis, Investigation. Ming Cheng: Resources, Visualization.

Declaration of competing interest

The authors declare that they have no known competing financial interests or personal relationships that could have appeared to influence the work reported in this paper.

Data availability

The data that has been used for the research was presented in the article

Acknowledgment

We gratefully appreciate the National Major Science and Technology Projects of China (2016ZX05034-001-005) and the National Natural Science Foundation of China (Grant No. 41972124). We also gratefully appreciate the PetroChina Southwest Oil and Gasfield Company for the data presented. Thanks to the Associate Editor Katz and reviewers for their careful review and constructive comments, which greatly improved the quality of the manuscript.

Appendix A

Table A1
Correlation between Al_2O_3 and investigated elements and remaining oxides

	V	Cr	Co	Ni	Cu	Ga	Rb	Sr	Zr	Nb	Ba	La	Yb
Al_2O_3	0.46	0.72	0.60	0.61	0.50	0.70	0.80	−0.61	0.36	0.38	0.60	0.12	0.22
	Hf	Ta	Pb	Th	U	CaO	Fe_2O_3	K_2O	MgO	MnO	Na_2O	P_2O_5	SiO_2
Al_2O_3	0.37	0.34	0.27	0.38	0.12	−0.90	0.57	0.84	0.23	−0.34	0.47	−0.75	0.79

References

Algeo, T.J., Ingall, E., 2007. Sedimentary Corg:P ratios, paleocean ventilation, and Phanerozoic atmospheric pO2. Palaeogeogr. Palaeoclimatol. Palaeoecol. 256, 130–155. https://doi.org/10.1016/j.palaeo.2007.02.029.

Algeo, T.J., Li, C., 2020. Redox classification and calibration of redox thresholds in sedimentary systems. Geochem. Cosmochim. Acta 287, 8–26. https://doi.org/10.1016/j.gca.2020.01.055.

Algeo, T.J., Liu, J., 2020. A re-assessment of elemental proxies for paleoredox analysis. Chem. Geol. 540 https://doi.org/10.1016/j.chemgeo.2020.119549.

Algeo, T.J., Lyons, T.W., 2006. Mo–total organic carbon covariation in modern anoxic marine environments: implications for analysis of paleoredox and paleohydrographic conditions. Paleoceanogr. Paleoclimatol. 21, 1016. https://doi.org/10.1029/2004PA001112.

Algeo, T.J., Rowe, H., 2021. Paleoceanographic applications of trace-metal concentration data. Chem. Geol. 324–325, 6–18. https://doi.org/10.1016/j.chemgeo.2011.09.002.

Algeo, T.J., Tribovillard, N., 2009. Environmental analysis of paleoceanographic systems based on molybdenum–uranium covariation. Chem. Geol. 268, 211–225. https://doi.org/10.1016/j.chemgeo.2009.09.001.

Arthur, M.A., Dean, W.E., 1998. Organic-matter production and preservation and evolution of anoxia in the Holocene Black Sea. Paleoceanography 13 (4), 395–411.

Arthur, M.A., Sageman, B.B., 1994. Marine black shales: depositional mechanisms and environments of ancient deposits. Annu. Rev. Earth Planet Sci. 22, 499–551. https://doi.org/10.1146/annurev.ea.22.050194.002435.

Beckmann, B., Flögel, S., Hofmann, P., Schulz, M., Wagner, T., 2005. Orbital forcing of Cretaceous river discharge in tropical Africa and ocean response. Nature 437 (7056), 241–244.

Bennett, W.W., Canfield, D.E., 2020. Redox-sensitive trace metals as paleoredox proxies: a review and analysis of data from modern sediments. Earth Sci. Rev. 204, 103175 https://doi.org/10.1016/j.earscirev.2020.103175.

Bishop, J.K.B., 1998. The barite-opal-organic carbon association in oceanic particulate matter. Nature 332, 341–343. https://doi.org/10.1038/332341a0.

Bohacs, K.M., Carroll, A.R., Neal, J.E., Mankiewicz, P.J., 2000. Lake-basin type, source potential, and hydrocarbon character: an integrated-sequence-stratigraphic–geochemical framework. In: GierlowskiKordesch, E.H., Kelts, K.R. (Eds.), Lake basins through space and time: AAPG Stud. Geol. 46, 334. https://doi.org/10.1306/St46706C1.

Bond, D.P.G., Wignall, P.B., 2010. Pyrite framboid study of marine Permian–Triassic boundary sections: a complex anoxic event and its relationship to contemporaneous mass extinction. GSA Bulletin 122, 1265–1279. https://doi.org/10.1130/B30042.1.

Brumsack, H.J., 2006. The trace metal content of recent organic carbon-rich sediments: implications for Cretaceous black shale formation. Palaeogeogr. Palaeoclimatol. Palaeoecol. 232, 344–361. https://doi.org/10.1016/j.palaeo.2005.05.011.

Cai, S., 1998. Some Fossil Freshwater Bivalves of the Jurassic Ziliujing Formation from Chongqing and Hechuan, Sichuan. Professional Papers of Stratigraphy and Palaeontology, p. 21 (in Chinese with English abstract).

Calvert, S.E., 1974. Deposition and diagenesis of silica in marine sediments. Pelagic sediments: on land and under the sea 1, 273–299. https://doi.org/10.1002/9781444304855.ch12.

Calvert, S.E., 1976. The mineralogy and geochemistry of near-shore sediments. Chemical oceanography 6, 187–280.

Calvert, S.E., Pedersen, T.F., 1993. Geochemistry of recent oxic and anoxic marine sediments: implications for the geological record. Mar. Geol. 113, 67–88. https://doi.org/10.1016/0025-3227(93)90150-T.

Caplan, M.L., Bustin, R.M., 1999. Palaeoceanographic controls on geochemical characteristics of organic-rich Exshaw mudrocks: role of enhanced primary production. Org. Geochem. 30, 161–188. https://doi.org/10.1016/S0146-6380(98)00202-2.

Chaikovskiy, I.I., Chaikovskaya, E.V., Korotchenkova, O.V., Chirkova, E.P., Utkina, T.A., 2019. Authigenic titanium and zirconium minerals at the verkhnekamskoe salt deposit. Geochem. Int. 57, 184–196.

Ding, Z.L., Sun, J.M., Yang, S.L., Liu, T.S., 2001. Geochemistry of the Pliocene red clay formation in the Chinese Loess Plateau and implications for its origin, source provenance and paleoclimate change. Geochem. Cosmochim. Acta 65, 901–913. https://doi.org/10.1016/S0016-7037(00)00571-8.

Dittmar, T., Kattner, G., 2003. The biogeochemistry of the river and shelf ecosystem of the Arctic Ocean: a review. Mar. Chem. 83, 103–120. https://doi.org/10.1016/S0304-4203(03)00105-1.

Dymond, J., Suess, E., Lyle, M., 1992. Barium in deep-sea sediment: a geochemical proxy for paleoproductivity. Paleoceanography 7, 163–181. https://doi.org/10.1029/92PA00181.

El Mourabet, M., Barakat, A., Zaghloul, M.N., El Baghdadi, M., 2018. Geochemistry of the Miocene Zoumi flysch thrust-top basin (External Rif, Morocco): new constraints on source area weathering, recycling processes, and paleoclimate conditions. Arabian J. Geosci. 11, 126.

Fedo, C.M., Wayne Nesbitt, H., Young, G.M., 1995. Unraveling the effects of potassium metasomatism in sedimentary rocks and paleosols, with implications for paleoweathering conditions and provenance. Geology 23, 921–924. https://doi.org/10.1130/0091-7613(1995)023<0921:UTEOPM>2.3.CO;2.

Floyd, P.A., Leveridge, B.E., Franke, W., Shail, R., Dörr, W., 1990. Provenance and depositional environment of Rhenohercynian synorogenic greywackes from the Giessen Nappe, Germany. Geol. Rundsch. 79, 611–626. https://doi.org/10.1007/BF01879205.

Ganeshram, R.S., Calvert, S.E., Pedersen, T.F., Cowie, G.L., 1999. Factors controlling the burial of organic carbon in laminated and bioturbated sediments off NW Mexico: implications for hydrocarbon preservation. Geochem. Cosmochim. Acta 63, 1723–1734. https://doi.org/10.1016/S0016-7037(99)00073-3.

Ganeshram, R.S., François, R., Commeau, J., Brown-Leger, S.L., 2003. An experimental investigation of barite formation in seawater. Geochem. Cosmochim. Acta 67, 2599–2605. https://doi.org/10.1016/S0016-7037(03)00164-9.

Gersten, J., Fainberg, V., Hetsroni, G., Shindler, Y., 2000. Kinetic study of the thermal decomposition of polypropylene, oil shale, and their mixture. Fuel 79 (13), 1679–1686.

Godderis, Y., Veizer, J., 2000. Tectonic control of chemical and isotopic composition of ancient oceans; the impact of continental growth. Am. J. Sci. 300, 434–461. https://doi.org/10.2475/ajs.300.5.434.

Goodarzi, F., Gentzis, T., 2018. Elemental concentration and organic petrology of unique liptinite-rich humic coal, canneloid shale, and cannel coal of Devonian age from

Arctic Canada. Chem. Geol. 485, 44–55. https://doi.org/10.1016/j.chemgeo.2018.03.035.
Goodarzi, F., Swaine, D.J., 1994. Paleoenvironmental and environmental aspects of B in coal. Geol. Surv. Can. Bull. 471, 76.
Guo, Z.W., Deng, K.L., Han, Y.H., 1996. The Formation and Evolution of Sichuan Basin. Geological Publishing House, Beijing (in Chinese).
Haddad, R.I., Martens, C.S., 1987. Biogeochemical cycling in an organic-rich coastal marine basin: 9. Sources and accumulation rates of vascular plant-derived organic material. Geochem. Cosmochim. Acta 51, 2991–3001. https://doi.org/10.1016/0016-7037(87)90372-3.
Hieronymus, B., Kotschoubey, B., Boulègue, J., 2001. Gallium behaviour in some contrasting lateritic profiles from Cameroon and Brazil. J. Geochem. Explor. 72 (2), 147–163.
Ibach, L.E.J., 1982. Relationship between sedimentation rate and total organic carbon content in ancient marine sediments. AAPG (Am. Assoc. Pet. Geol.) Bull. 66, 170–188. https://doi.org/10.1306/03B59A5D-16D1-11D7-8645000102C1865D.
Ingall, E., Kolowith, L., Lyons, T., Hurtgen, M., 2005. Sediment carbon, nitrogen and phosphorus cycling in an anoxic fjord, Effingham Inlet, British Columbia[J]. Am. J. Sci. 305, 240–258. https://doi.org/10.2475/ajs.305.3.240.
Ingall, E.D., Van Cappellen, P., 1990. Relation between sedimentation rate and burial of organic phosphorus and organic carbon in marine sediments. Geochem. Cosmochim. Acta 54 (2), 373–386.
Jones, B., Manning, D.A.C., 1994. Comparison of geochemical indices used for the interpretation of palaeoredox conditions in ancient mudstones. Chem. Geol. 111, 111–129. https://doi.org/10.1016/0009-2541(94)90085-X.
Kidwell, S.M., 1991. The stratigraphy of shell concentrations. In: Allison, P.A., Briggs, D.E.G. (Eds.), Taphonomy, Releasing the Data Locked in the Fossil Record. Plenum Press, New York, pp. 211–290.
Lei, W.Z., Chen, D.X., Zhang, R., Liu, Z.Y., Zhang, S.M., 2021. Lithological combination types and characteristics of continental shale strata in the second sub-member of Da'anzhai in central sichuan. Earth Sci. 46 (10), 3657–3672. https://doi.org/10.3799/dqkx.2021.023 (in Chinese with English abstract).
Li, X., 2016. Study on cyclic stratigraphy of Da'anzhai member in Gong39 well Area, central sichuan. In: Master Thesis: Southwest Petroleum University (in Chinese with English abstract).
Liang, H., Xu, G., Xu, F., Yu, Q., Liang, J., Wang, D., 2020. Paleoenvironmental evolution and organic matter accumulation in an oxygen-enriched lacustrine basin: a case study from the Laizhou Bay Sag, southern Bohai Sea (China). Int. J. Coal Geol. 217, 103318 https://doi.org/10.1016/j.coal.2019.103318.
Lin, S., Shen, S., Zhou, A., Lyu, H.M., 2020. Assessment and management of lake eutrophication: a case study in Lake Erhai, China. Sci. Total Environ. 751, 141618 https://doi.org/10.1016/j.scitotenv.2020.141618.
Liu, J., Cao, J., Hu, G., Wang, Y., Yang, R., Liao, Z., 2020. Water-level and redox fluctuations in a Sichuan Basin lacustrine system coincident with the Toarcian OAE. Palaeogeogr. Palaeoclimatol. Palaeoecol. 558, 109942 https://doi.org/10.1016/j.palaeo.2020.109942.
Liu, S., Yang, Y., Deng, B., Zhong, Y., Wen, L., Sun, W., Li, Z., Jansa, L.B., Li, J., Song, J.M., Zhang, X.H., Peng, H.L., 2020. Tectonic evolution of the Sichuan basin, southwest China. Earth Sci. Rev. 213, 103470 https://doi.org/10.1016/j.earscirev.2020.103470.
Liu, Z., Chen, D., Lei, W., Liu, Y., Xie, G., Dang, W., Lv, X., Li, S., Yuan, S., 2022. Controls of the paleoenvironment on differential organic matter enrichment of lacustrine fine-grained rocks: a case study of the Jurassic Da'anzhai Member, central Sichuan Basin, SW China. J. Asian Earth Sci. 236, 105319 https://doi.org/10.1016/j.jseaes.2022.105319.
Liu, Z., Chen, D., Zhang, J., Lyu, X., Wang, Z., Liao, W.H., Shi, X., Tang, J., Xie, G., 2019. Pyrite morphology as an indicator of paleoredox conditions and shale gas content of the Longmaxi and Wufeng shales in the Middle Yangtze area, South China. Minerals 9, 428. https://doi.org/10.3390/min9070428.
Lu, Y., Huang, C., Jiang, S., Zhang, J., Lu, Y., Liu, Y., 2019. Cyclic late Katian through Hirnantian glacioeustasy and its control of the development of the organic-rich Wufeng and Longmaxi shales, South China. Palaeogeogr. Palaeoclimatol. Palaeoecol. 526, 96–109. https://doi.org/10.1016/j.palaeo.2019.04.012.
Mansour, A., Wagreich, M., Gentzis, T., Ocubalidet, S., Tahoun, S.S., Elewa, A.M.T., 2020. Depositional and organic carbon-controlled regimes during the Coniacian-Santonian event: first results from the southern Tethys (Egypt). Mar. Petrol. Geol. 115, 104285 https://doi.org/10.1016/j.marpetgeo.2020.104285.
McAlister, J.A., Orians, K.J., 2015. Dissolved gallium in the beaufort sea of the western arctic ocean: a GEOTRACES cruise in the international polar year. Mar. Chem. 177, 101–109. https://doi.org/10.1016/j.marchem.2015.05.007.
Morel, F.M.M., Price, N.M., 2003. The biogeochemical cycles of trace metals in the oceans. Science 300, 944–947. https://doi.org/10.1126/science.1083545.
Morford, J.L., Emerson, S.R., Breckel, E.J., Kim, S.H., 2005. Diagenesis of oxyanions (V, U, Re, and Mo) in pore waters and sediments from a continental margin. Geochem. Cosmochim. Acta 69, 5021–5032. https://doi.org/10.1016/j.gca.2005.05.015.
Morford, J.L., Martin, W.R., Carney, C.M., 2009. Uranium diagenesis in sediments underlying bottom waters with high oxygen content. Geochem. Cosmochim. Acta 73, 2920–2937. https://doi.org/10.1016/j.gca.2009.02.014.
Müller, P.J., Suess, E., 1979. Productivity, sedimentation rate, and sedimentary organic matter in the oceans—I. Organic carbon preservation. Deep Sea Research Part A. Oceanographic Research Papers 26 (12), 1347–1362.
Murphy, A.E., Sageman, B.B., Hollander, D.J., Lyons, T.W., Brett, C.E., 2000. Black shale deposition and faunal overturn in the Devonian Appalachian Basin: clastic starvation, seasonal water-column mixing, and efficient biolimiting nutrient recycling. Paleoceanography 15, 280–291. https://doi.org/10.1029/1999PA000445.
Nesbitt, H.W., Young, G.M., 1982. Early Proterozoic climates and plate motions inferred from major element chemistry of lutites. Nature 299, 715–717. https://doi.org/10.1038/299715a0.
Nesbitt, H.W., Young, G.M., McLennan, S.M., Keays, R.R., 1996. Effects of chemical weathering and sorting on the petrogenesis of siliciclastic sediments, with implications for provenance studies. J. Geol. 104, 525–542. https://doi.org/10.1086/629850.
Pan, J.F., Wang, W.X., 2004. Differential uptake of dissolved and particulate organic carbon by the marine mussel Perna viridis. Limnol. Oceanogr. 49, 1980–1991. https://doi.org/10.4319/lo.2004.49.6.1980.
Pang, X.Q., Li, Q.W., Chen, J.F., Li, M.W., Pang, H., 2014. Recovery method of original TOC and its application in source rocks at high mature - over mature stage in deep petroliferous basins. J. Palaeogeogr. 16 (6), 769–789 (in Chinese with English abstract).
Plank, T., Langmuir, C.H., 1998. The chemical composition of subducting sediment and its consequences for the crust and mantle. Chem. Geol. 145, 325–394. https://doi.org/10.1016/S0009-2541(97)00150-2.
Poulton, S.W., Canfield, D.E., 2011. Ferruginous conditions: a dominant feature of the ocean through Earth's history. Elements 7, 107–112. https://doi.org/10.2113/gselements.7.2.107.
Prokopenko, A.A., Karabanov, E.B., Williams, D.F., Kuzmin, M.I., Shackleton, N.J., Crowhurst, S.J., Peck, J.A., Gvozdkov, A.N., King, J.W., 2001. Biogenic silica record of the lake baikal response to climatic forcing during the brunhes. Quat. Res. 55, 123–132. https://doi.org/10.1006/qres.2000.2212.
Ratcliffe, K.T., Wright, A.M., Montgomery, P., Palfrey, A., Vonk, A., Vermeulen, J., Barrett, M., 2010. Application of chemostratigraphy to the mungaroo formation, the gorgon field, offshore northwest Australia. APPEA Journal 2010 50th Anniversary Issue 371–388.
Redfield, A.C., 1958. The biological control of chemical factors in the environment. Am. Sci. 46, 230A+205–221. https://www.jstor.org/stable/27827150.
Rimmer, S.M., Thompson, J.A., Goodnight, S.A., Robl, T.L., 2004. Multiple controls on the preservation of organic matter in Devonian–Mississippian marine black shales: geochemical and petrographic evidence. Palaeogeogr. Palaeoclimatol. Palaeoecol. 215, 125–154. https://doi.org/10.1016/j.palaeo.2004.09.001.
Roden, E.E., Leonardo, M.R., Ferris, F.G., 2002. Immobilization of strontium during iron biomineralization coupled to dissimilatory hydrous ferric oxide reduction. Geochem. Cosmochim. Acta 66, 2823–2839. https://doi.org/10.1016/S0016-7037(02)00878-5.
Ross, D.J.K., Bustin, R.M., 2009. Investigating the use of sedimentary geochemical proxies for paleoenvironment interpretation of thermally mature organic-rich strata: examples from the Devonian–Mississippian shales, Western Canadian Sedimentary Basin. Chem. Geol. 260, 1–19. https://doi.org/10.1016/j.chemgeo.2008.10.027.
Roy, D.K., Roser, B.P., 2013. Climatic control on the composition of carboniferous–permian gondwana sediments, khalaspir basin, Bangladesh. Gondwana Res. 23, 1163–1171.
Sageman, B.B., Murphy, A.E., Werne, J.P., Straeten, C.A.V., Hollander, D.J., Lyons, T.W., 2003. A tale of shales: the relative roles of production, decomposition, and dilution in the accumulation of organic-rich strata, Middle–Upper Devonian, Appalachian basin. Chem. Geol. 195, 229–273. https://doi.org/10.1016/S0009-2541(02)00397-2.
Schoepfer, S.D., Shen, J., Wei, H., Tyson, R.V., Ingall, E., Algeo, T.J., 2015. Total organic carbon, organic phosphorus, and biogenic barium fluxes as proxies for paleomarine productivity. Earth Sci. Rev. 149, 23–52. https://doi.org/10.1016/j.earscirev.2014.08.017.
Shen, J., Schoepfer, S.D., Feng, Q., Zhou, L., Yu, J., Song, H., Wei, H., Algeo, T.J., 2015. Marine productivity changes during the end-Permian crisis and Early Triassic recovery. Earth Sci. Rev. 149, 136–162. https://doi.org/10.1016/j.earscirev.2014.11.002.
Shiller, A.M., Frilot, D.M., 1996. The geochemistry of gallium relative to aluminum in Californian streams. Geochem. Cosmochim. Acta 60, 1323–1328. https://doi.org/10.1016/0016-7037(96)00002-6.
Simon, A., Poulicek, M., Velimirov, B., MacKenzie, F.T., 1994. Comparison of anaerobic and aerobic biodegradation of mineralized skeletal structures in marine and estuarine conditions. Biogeochemistry 25, 167–195. https://doi.org/10.1007/BF00024391.
Smolarek, J., Trela, W., Bond, D.P.G., Marynowski, L., 2017. Lower Wenlock black shales in the northern Holy Cross Mountains, Poland: sedimentary and geochemical controls on the Ireviken Event in a deep marine setting. Geol. Mag. 154, 247–264. https://doi.org/10.1017/S0016756815001065.
Sternberg, E., Tang, D., Ho, T.Y., Jeandel, C., Morel, F.M.M., 2005. Barium uptake and adsorption in diatoms. Geochem. Cosmochim. Acta 69, 2745–2752. https://doi.org/10.1016/j.gca.2004.11.026.
Taylor, S.R., McLennan, S.M., 1985. The Continental Crust: its Composition and Evolution. Blackwell Scientific Publication, Oxford.
Tribovillard, N., Algeo, T.J., Lyons, T., Riboulleau, A., 2006. Trace metals as paleoredox and paleoproductivity proxies: an update. Chem. Geol. 232, 12–32. https://doi.org/10.1016/j.chemgeo.2006.02.012.
Tyrrell, T., 1999. The relative influences of nitrogen and phosphorus on oceanic primary production. Nature 400, 525–531. https://doi.org/10.1038/22941.
Tyson, R.V., 2001. Sedimentation rate, dilution, preservation and total organic carbon: some results of a modelling study. Org. Geochem. 32, 333–339. https://doi.org/10.1016/S0146-6380(00)00161-3.
Tyson, R.V., Pearson, T.H., 1991. Modern and Ancient Continental Shelf Anoxia: an Overview, vol. 58. Geological Society, London, Special Publications, pp. 1–24. https://doi.org/10.1144/GSL.SP.1991.058.01.01.

Wang, Q., Chen, D., Wang, F., Gao, X., Zou, Y., Tian, Z., Li, S., Chang, S., Yao, D., 2021. Origin and distribution of an under-pressured tight sandstone reservoir: the Shaximiao formation, central Sichuan Basin. Mar. Petrol. Geol. 132, 105208 https://doi.org/10.1016/j.marpetgeo.2021.105208.

Wang, Q., Liang, B., Kan, Z., 2006. Carbon and oxygen isotopic compositions of lacustrine carbonates of the Early Jurassic Ziliujing Formation in the Sichuan Basin and their paleolimnological significance. Mineral. Petrol. 26, 87–91 (in Chinese with English abstract).

Wei, W., Algeo, T.J., 2020. Elemental proxies for paleosalinity analysis of ancient shales and mudrocks. Geochem. Cosmochim. Acta 287, 341–366. https://doi.org/10.1016/j.gca.2019.06.034.

Wei, W., Algeo, T.J., Lu, Y., Lu, Y., Liu, H., Zhang, S., Peng, L., Zhang, J., Chen, L., 2018. Identifying marine incursions into the Paleogene Bohai Bay Basin lake system in northeastern China. Int. J. Coal Geol. 200, 1–17. https://doi.org/10.1016/j.coal.2018.10.001.

Wignall, P.B., Twitchett, R.J., 1996. Oceanic anoxia and the end Permian mass extinction. Science 272, 1155–1158.

Wilkin, R.T., Barnes, H.L., 1997. Formation processes of framboidal pyrite. Geochem. Cosmochim. Acta 61 (2), 323–339. https://doi.org/10.1126/science.272.5265.1155.

Xiao, Z.L., Chen, S.J., Zhang, S.M., Zhang, R., Zhu, Z.Y., Lu, J.G., Li, Y., Yin, X.D., Tang, L. X., Liu, Z.H., Lin, Z.H., 2021. Sedimentary environment and model for lacustrine organic matter enrichment: lacustrine shale of the Early Jurassic Da'anzhai Formation, central Sichuan Basin, China. J. Palaeogeogr. 10 (4), 584–601. https://doi.org/10.1016/j.jop.2021.09.002.

Xie, W., Yang, W., Yang, G., Yang, Y., Xie, Z., Hui, J., Zhu, Q., Sheng, J., 2010. Pore structure features of sandstone reservoirs in the upper triassic Xujiahe Formation in the central part of Sichuan Basin. Nat. Gas Geosci. 21 (3), 435–440 (in Chinese with English abstract).

Xu, H., Paerl, H.W., Qin, B., Zhu, G.W., Guang, G.A., 2010. Nitrogen and phosphorus inputs control phytoplankton growth in eutrophic Lake Taihu, China. Limnol. Oceanogr. 55 (1), 420–432.

Xu, Q., Liu, B., Ma, Y., Song, X., Wang, Y., Chen, Z., 2017. Geological and geochemical characterization of lacustrine shale: a case study of the Jurassic Da'anzhai member shale in the central Sichuan Basin, southwest China. J. Nat. Gas Sci. Eng. 47, 124–139. https://doi.org/10.1016/j.jngse.2017.09.008.

Xu, S.C., Hu, H.B., Zhang, P., Wang, Q.C., Kang, J., Miao, Q., 2020. Major and trace elements in mid-Eocene lacustrine oil shales of the Fushun Basin, NE China: concentration features and paleolimnological implications. Mar. Petrol. Geol. 121, 104610 https://doi.org/10.1016/j.marpetgeo.2020.104610.

Xu, S.C., Liu, Z.J., Dong, Q.S., Liu, R., Meng, Q.T., Hu, X.F., 2013. Characteristics and origin of organic geochemistry from the Eocene source rocks, Fushun basin, Liaoning Province. J. China Inst. Min. Technol. 42, 790–800. https://doi.org/10.13247/j.cnki.jcumt.2013.05.014.

Yang, W., Zuo, R., Chen, D., Jiang, Z., Guo, L., Liu, Z., Chen, R., Zhang, Y., Zhang, Z., Song, Y., Luo, Q., Wang, Q., Wang, J., Lei, C., Li, C., Li, Y., Zhang, C., 2019. Climate and tectonic-driven deposition of sandwiched continental shale units: new insights from petrology, geochemistry, and integrated provenance analyses (the western Sichuan subsiding Basin, Southwest China). Int. J. Coal Geol. 211, 103227 https://doi.org/10.1016/j.coal.2019.103227.

Yang, Y.M., Huang, D., Yang, G., Li, Y., Dai, H., Bai, R., 2019. Geological conditions to form lacustrine facies shale oil and gas of Jurassic Da'anzhai Member in Sichuan Basin and exploration directions. Natural Gas Exploration and Development 42 (2), 1–12 (in Chinese with English abstract).

Zhang, F., Zhou, Y., Ge, R., Hu, X., Xiong, C., Yi, W., 2018. A new type of lacustrine ichnofossils from the Lower Jurassic Ziliujing Formation in Wanzhou of Chongqing and its paleoenvironmental significances. Acta Palaeontol. Sin. 57 (2), 228–236 (in Chinese with English abstract).

Zheng, R., Guo, R., Liang, X., Chang, H., Lu, B., 2016. Characteristics and evaluation of reservoir spaces of shale gas (oil) in Da'anzhai Member of Ziliujing Formation in Sichuan Basin. Lithologic Reservoirs 28 (1), 16–29 (in Chinese with English abstract).